

# Information-Guided Noise Allocation for Efficient Diffusion Training

Gabriel Raya<sup>\*1,2</sup> Bac Nguyen<sup>3</sup> Georgios Batzolis<sup>4</sup> Yuhta Takida<sup>3</sup> Dejan Stancevic<sup>5</sup> Naoki Murata<sup>3</sup>  
Chieh-Hsin Lai<sup>3</sup> Yuki Mitsufuji<sup>3,6</sup> Luca Ambrogioni<sup>5</sup>

## Abstract

Training diffusion models typically relies on manually tuned noise schedules, which can waste computation on weakly informative noise regions and limit transfer across datasets, resolutions, and representations. We revisit noise schedule allocation through an information-theoretic lens and propose the conditional entropy rate of the forward process as a theoretically grounded, data-dependent diagnostic for identifying suboptimal noise-level allocation in existing schedules. Based on these insight, we introduce INFONOISE, a principled data-adaptive training noise schedule that replaces heuristic schedule design with an information-guided noise sampling distribution derived from entropy-reduction rates estimated from denoising losses already computed during training. Across natural-image benchmarks, INFONOISE matches or surpasses tuned EDM-style schedules, in some cases with a substantial training speedup (about  $1.4\times$  on CIFAR-10). On discrete datasets, where standard image-tuned schedules exhibit significant mismatch, it reaches superior quality in up to  $3\times$  fewer training steps. Overall, INFONOISE makes noise scheduling data-adaptive, reducing the need for per-dataset schedule design as diffusion models expand across domains.

## 1. Introduction

Diffusion models (Sohl-Dickstein et al., 2015) have become a standard approach to high-quality generative modeling, with strong results across images and other modalities (Ho et al., 2020; Song & Ermon, 2019; Song et al., 2020; Karras et al., 2022; Lai et al., 2025; Esser et al., 2024). Despite this progress, training remains sensitive to a practical choice: the *training noise schedule* (hereafter, *noise schedule*), which

<sup>\*</sup>Work partially done during an internship at Sony AI, Tokyo, Japan. <sup>1</sup>Jheronimus Academy of Data Science <sup>2</sup>Tilburg University. <sup>3</sup>Sony AI <sup>4</sup>University of Cambridge <sup>5</sup>Radboud University <sup>6</sup>Sony Group Corporation. Correspondence to: Gabriel Raya <g.raya@tue.nl,gaboraya@gmail.com>.

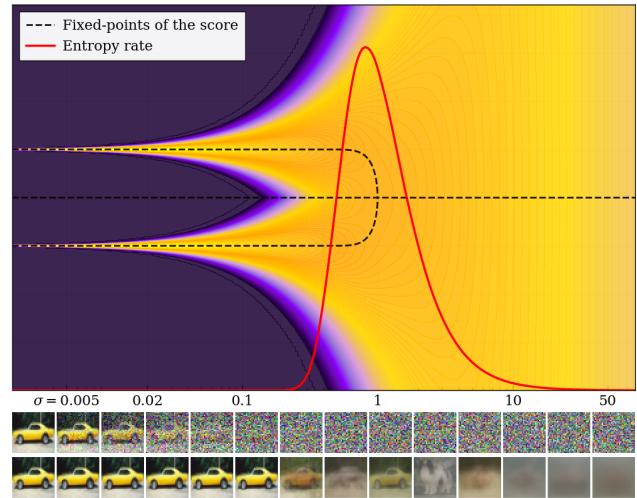


**Figure 1. Uncertainty collapses in an intermediate noise range.** **Top.** Two-point toy data ( $-1, +1$ ) with additive Gaussian corruption at noise level  $\sigma$ . As  $\sigma$  decreases (moving right to left), the *optimal* denoising field bifurcates: a single symmetric stable fixed point near 0 splits into two stable branches near  $\pm 1$  (dotted curves), marking a decision window where the posterior transitions from averaging over modes to committing to one. The **red curve** overlays the toy entropy-rate profile, peaking in this same window where uncertainty resolves most rapidly. Background shows the log-density of  $x_\sigma$  (yellow high, purple low). In this view, the bifurcation marks the onset of symmetry breaking, coinciding with the noise range where uncertainty collapses fastest. **Bottom.** CIFAR-10 optimal-denoiser diagnostic (Section A.2). Each column shows a noisy input (top) and its optimal denoised prediction (bottom), with the most pronounced qualitative change concentrated at intermediate  $\sigma$ , mirroring the toy decision window.

determines how optimization effort is distributed across noise levels along the corruption path. In practice, schedules are still selected from hand-designed families and tuned to a particular dataset, resolution, or representation (Nichol & Dhariwal, 2021; Karras et al., 2022; Hoogeboom et al., 2023; Chen, 2023; Teng et al., 2023; Karras et al., 2024; Kingma & Gao, 2023; Esser et al., 2024). However, such tuning often fails to transfer. A schedule that performs well in one setting can oversample noise regimes where additional updates carry little learning signal in another, wasting compute and motivating repeated retuning (Austin et al., 2021; Lee et al., 2024). This raises a natural question: *can we make noise scheduling data-adaptive, avoiding per-dataset tuning while retaining training efficiency?*

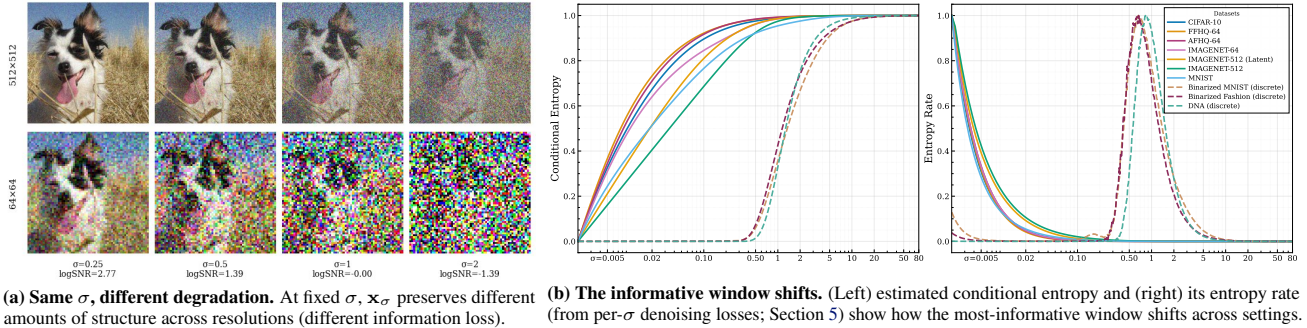


Figure 2. Fixed noise schedules do not transfer across datasets, resolutions, and representations. (a) At the same noise level  $\sigma$ , images at different resolutions can lose markedly different structure; equal  $\sigma$  need not imply comparable degradation. (b) Entropy-rate profiles vary across datasets and representations, indicating that the noise range where uncertainty drops fastest is *data-dependent*. Fixed schedules can therefore over-sample near-flat regions and under-sample the informative window where learning has the highest leverage.

A key observation is that uncertainty about the clean sample resolves unevenly along the corruption path. Most of the reduction occurs in an intermediate *informative window*, where denoising has the highest leverage (Figure 1). In the toy example (top), this window is explicit: as  $\sigma$  decreases, the optimal denoising field bifurcates. At high noise there is a single symmetric stable fixed point near 0, while below a critical noise level it splits into two stable branches near  $\pm 1$ , reflecting the posterior’s transition from averaging over modes to committing to one. The same noise range also contains the sharpest drop in posterior uncertainty, aligning with the onset of symmetry breaking and pattern formation (Raya & Ambrogioni, 2024; Biroli et al., 2024; Li & Chen, 2024; Sinha & Kooloth, 2025; Collier, 1996). This is not only a toy effect: on CIFAR-10, the ideal denoiser shows its most pronounced qualitative change at intermediate  $\sigma$  (bottom of Figure 1). Crucially, the location and width of the informative window are not fixed across settings. Figure 2 highlights two sources of mismatch that undermine transfer. At the same noise level  $\sigma$ , corrupted inputs can retain different amounts of structure across resolutions, implying different effective information loss. The noise range where uncertainty drops fastest also shifts across datasets and representations. Since the noise schedule determines how often each  $\sigma$  is used during training, an effective schedule should concentrate updates where uncertainty is reduced most efficiently, rather than spending many updates at extremes where the signal is either too weak (high noise) or already saturated (low noise).

A natural way to formalize this phenomenon is via the conditional entropy  $H[\mathbf{x}_0 | \mathbf{x}_\sigma]$ , which quantifies the remaining uncertainty about the clean sample  $\mathbf{x}_0$  given a noisy observation  $\mathbf{x}_\sigma$  at level  $\sigma$ . We refer to its slope along the corruption path as the *conditional entropy rate* (entropy rate). When this entropy rate signal concentrates in a narrow intermediate range, it identifies an informative window where allocating computation most directly accelerates learning. This yields

a direct criterion for schedule design: allocate sampling mass in proportion to the entropy-rate profile, concentrating updates where uncertainty drops fastest while still covering the rest of the path. If a schedule allocates mass away from this window, equal compute yields slower progress. In this view, hand-designed schedule families amount to guessing where this high-leverage region lies and how broadly to cover it, which becomes brittle when the informative window shifts across settings.

To turn this principle into an adaptive training schedule, we need an entropy-rate estimate available during training. For Gaussian corruption, classical information identities relate how information evolves along the noise path to the minimum achievable denoising error (Guo et al., 2005; Palomar & Verdú, 2005). Recent diffusion work has used this link to construct information profiles for inference-time discretization from pre-trained models (Stancevic et al., 2025). In our setting, the same link makes the entropy-rate profile estimable from the per-noise denoising losses already computed during training, revealing where conditional uncertainty is being resolved most rapidly.

We introduce INFONOISE, a data-adaptive training noise schedule that steers optimization toward informative noise levels. INFONOISE updates only how often each noise level is sampled, using an entropy-rate estimate derived from denoising losses computed during optimization. This makes INFONOISE a drop-in replacement for fixed schedules: the diffusion objective, model parameterization, and loss weighting can be kept unchanged. Unlike entropic-time methods (e.g. (Stancevic et al., 2025)), which reparameterize inference-time discretization of a pre-trained model, INFONOISE operates during training by reallocating optimization effort toward informative noise levels. We evaluate INFONOISE on continuous images and discrete modalities. On natural-image benchmarks, INFONOISE matches carefully tuned EDM-style schedules at equal compute, suggesting that established image schedules already approximate

an information-efficient allocation. On discrete benchmarks, where the informative band shifts more sharply, INFO-NOISE reaches the same target quality in up to  $3\times$  fewer training steps.

**Contributions.** We make two contributions. First, we cast training noise scheduling as allocating a finite sampling budget along the Gaussian corruption path, and show that entropy-rate profiles identify a data-dependent intermediate window where training updates have the highest leverage, clarifying when hand-designed schedules misallocate compute as this window shifts. Second, we propose INFO-NOISE, an online, data-adaptive schedule that estimates this signal from per-noise denoising losses during optimization and updates only how often each noise level is sampled; the objective, parameterization, and loss weighting can be kept unchanged, making it a drop-in replacement for fixed schedules. We validate INFO-NOISE across continuous and discrete benchmarks, improving time-to-quality when the informative window shifts sharply while remaining competitive on natural images where schedules are already highly optimized.

## 2. Preliminaries

This section introduces notation and background needed to view noise scheduling as an allocation problem. Section 2.1 reviews the variance-exploding (VE) Gaussian corruption process in the EDM (Karras et al., 2022) framework, the corresponding reverse-time dynamics, and the standard denoiser-based training objective. Section 2.2 then introduces information-theoretic measures of denoising difficulty along the Gaussian channel. We recall the I-MMSE identity (Guo et al., 2005) that links the *entropy-rate* to the irreducible denoising error, which we will use to identify informative noise regions and construct an adaptive schedule.

### 2.1. Gaussian corruption and reverse dynamics

Diffusion models are probabilistic generative models that generate data by learning to invert a fixed Gaussian corruption process. Following EDM (Karras et al., 2022), we adopt the noise coordinate  $\sigma \in [\sigma_{\min}, \sigma_{\max}]$  and define the variance-exploding (VE) channel

$$\mathbf{x}_\sigma = \mathbf{x}_0 + \sigma \boldsymbol{\varepsilon}, \quad \mathbf{x}_0 \sim p_{\text{data}}, \quad \boldsymbol{\varepsilon} \sim \mathcal{N}(\mathbf{0}, \mathbf{I}). \quad (1)$$

Let  $p(\mathbf{x}; \sigma)$  denote the marginal distribution of  $\mathbf{x}_\sigma$ . In continuous time, the VE channel in Equation (1) has the same marginals as the Itô SDE

$$d\mathbf{x}_\sigma = \sqrt{2\sigma} d\mathbf{W}_\sigma, \quad (2)$$

where  $\mathbf{W}_\sigma$  is a standard  $d$ -dimensional Wiener process indexed by  $\sigma$ . This forward SDE admits stochastic and deterministic reverse-time dynamics (Anderson, 1982; Song

et al., 2020):

$$d\mathbf{x}_\sigma = -2\sigma \nabla_{\mathbf{x}_\sigma} \log p(\mathbf{x}_\sigma; \sigma) d\sigma + \sqrt{2\sigma} d\bar{\mathbf{W}}_\sigma, \quad (3)$$

$$\frac{d\mathbf{x}_\sigma}{d\sigma} = -\sigma \nabla_{\mathbf{x}_\sigma} \log p(\mathbf{x}_\sigma; \sigma). \quad (4)$$

Both reverse-time dynamics depend on the data only through the score  $\nabla_{\mathbf{x}_\sigma} \log p(\mathbf{x}_\sigma; \sigma)$ . Rather than learning the score directly, implementations typically learn a noise-conditioned denoiser  $\hat{\mathbf{x}}_\theta(\mathbf{x}_\sigma; \sigma)$  (or an equivalent parameterization that is deterministically convertible to an  $\mathbf{x}_0$ -estimate), together with a fixed per-noise weighting or preconditioning rule (Ho et al., 2020; Karras et al., 2022; Kingma & Gao, 2023). In practice, many training objectives take the form of a Monte Carlo estimator over  $\sigma$ :

$$\mathcal{L}_w(\mathbf{x}_0) = \mathbb{E}_{\sigma \sim \pi(\sigma)} \mathbb{E}_\varepsilon \left[ w(\sigma) \|\mathbf{x}_0 - \hat{\mathbf{x}}_\theta(\mathbf{x}_\sigma; \sigma)\|_2^2 \right]. \quad (5)$$

Here  $\pi(\sigma)$  is the sampling density that determines how often each noise level is sampled during optimization; we call  $\pi$  the *training noise schedule*. Many diffusion works instead use a time index  $t$  together with a monotone *noise-level parameterization*  $t \mapsto \sigma(t)$ . This choice implicitly induces a schedule on  $\sigma$  through the pushforward density (for invertible  $t \mapsto \sigma(t)$ )

$$\pi(\sigma) = \pi_t(t(\sigma)) \left| \frac{dt}{d\sigma} \right|. \quad (6)$$

Here  $\pi_t$  denotes the sampling density in the auxiliary coordinate  $t$ , and  $\pi(\sigma)$  is its pushforward density over  $\sigma$ . Since parameterizations and heuristics ultimately act by reallocating training mass along  $\sigma$ , we treat  $\pi(\sigma)$  as the primary object and reserve *noise-level parameterization* for a monotone index map. The deterministic factor  $w(\sigma) \geq 0$  is the per-noise *loss weight*, fixed by the objective and separate from  $\pi$ . Differences across training recipes correspond to changing  $\pi$ ,  $w$ , or both. For allocation, it is convenient to combine them into the *effective weight*

$$\phi(\sigma) \triangleq \pi(\sigma) w(\sigma), \quad (7)$$

which determines how strongly each noise region contributes to the regression objective (Equation (5)).

At inference time, generation discretizes  $[\sigma_{\min}, \sigma_{\max}]$  into a grid  $\sigma_{\max} = \sigma_0 > \dots > \sigma_N = \sigma_{\min}$  and integrates the reverse dynamics from  $\sigma_{\max}$  to  $\sigma_{\min}$ . This produces a sequence of denoising steps, so model errors at particular noise levels propagate to later steps and may compound, degrading the final sample. Good generation therefore depends on the model being reliable along the noise path, especially in the regions where uncertainty is resolved most rapidly. Section 2.2 formalizes denoising difficulty along the noise path using information-theoretic quantities induced by the Gaussian channel.

## 2.2. Information-theoretic denoising difficulty

To characterize the intrinsic difficulty of estimating  $\mathbf{x}_0$  from  $\mathbf{x}_\sigma$  across noise levels, we study conditional uncertainty under the VE channel in Equation (1) and relate its variation along  $\sigma$  to Bayes-optimal mean-squared error via I-MMSE.

### Conditional uncertainty along the Gaussian channel.

Under Gaussian corruption in Equation (1), the remaining uncertainty about  $\mathbf{x}_0$  after observing  $\mathbf{x}_\sigma$  is measured by the conditional entropy

$$H[\mathbf{x}_0 | \mathbf{x}_\sigma] \triangleq -\mathbb{E}_{p(\mathbf{x}_0, \mathbf{x}_\sigma)}[\log p(\mathbf{x}_0 | \mathbf{x}_\sigma)], \quad (8)$$

where this is a function of  $\sigma$  determined by the data distribution and the corruption channel. Equivalently, the mutual information satisfies

$$I[\mathbf{x}_0; \mathbf{x}_\sigma] = H[\mathbf{x}_0] - H[\mathbf{x}_0 | \mathbf{x}_\sigma], \quad (9)$$

so tracking  $H[\mathbf{x}_0 | \mathbf{x}_\sigma]$  is equivalent to tracking  $I[\mathbf{x}_0; \mathbf{x}_\sigma]$  up to the constant  $H[\mathbf{x}_0]$ .

**Bayes-optimal denoising error.** The intrinsic denoising difficulty at noise level  $\sigma$  is captured by the Bayes MMSE

$$\text{mmse}(\sigma) \triangleq \mathbb{E}[\|\mathbf{x}_0 - \mathbb{E}[\mathbf{x}_0 | \mathbf{x}_\sigma]\|_2^2], \quad (10)$$

which lower-bounds the mean-squared error of any estimator  $\hat{\mathbf{x}}_0(\mathbf{x}_\sigma; \sigma)$  (Lehmann & Casella, 1998). The posterior mean  $\mathbb{E}[\mathbf{x}_0 | \mathbf{x}_\sigma]$  is the unique MSE-optimal denoiser.

**Entropy-rate identity (I-MMSE).** For the Gaussian channel in Equation (1), the classical I-MMSE identities link the variation of conditional entropy to the Bayes-optimal denoising error (Guo et al., 2005; Palomar & Verdú, 2005). In the VE noise coordinate, this yields the pathwise entropy-rate identity (Stancevic et al., 2025)

$$\frac{d}{d\sigma} H[\mathbf{x}_0 | \mathbf{x}_\sigma] = \frac{\text{mmse}(\sigma)}{\sigma^3} \geq 0. \quad (11)$$

We refer to the left-hand side as the *conditional-entropy rate* along  $\sigma$ . Large values identify noise regions where conditional entropy is most sensitive to  $\sigma$ ; along denoising (decreasing  $\sigma$ ), these are the regions where uncertainty drops most rapidly in magnitude and training updates have the highest leverage.

Equation (11) reduces information change along the Gaussian channel to a one-dimensional profile over noise levels, capturing where denoising is intrinsically hardest in the Bayes sense. This suggests a principled way to choose *how often* to visit each noise level during training: estimate the profile online from per-noise denoising losses and concentrate sampling where uncertainty changes most rapidly, while still covering the full path.

## 3. Information-guided noise scheduling

Section 2.2 relates the change in conditional entropy along the Gaussian path to Bayes-optimal denoising difficulty via Equation 11. This defines a data- and channel-dependent profile over  $[\sigma_{\min}, \sigma_{\max}]$  that highlights where conditional uncertainty changes most sharply. We use an online estimate of this profile to set how often each noise level is sampled during training.

We convert the estimated profile into a target emphasis  $\rho(\sigma)$  by regularizing and normalizing it, then choose a sampling schedule  $\pi(\sigma)$  so that, under the weighted objective in Equation (5), the effective emphasis matches  $\rho(\sigma)$  up to normalization. Since the loss weight is fixed by the training objective, this step adjusts only the sampling distribution.

### 3.1. From entropy rate to a target allocation

We turn the conditional-entropy rate along the noise path into a target allocation over noise levels. As  $\sigma \rightarrow 0$ , the raw profile can be dominated by a universal low-noise tail induced by the Gaussian channel geometry, so we form  $\rho$  from a regularized version of the signal (Section 3.3).

Define

$$\dot{H}[\mathbf{x}_0 | \mathbf{x}_\sigma] \triangleq \frac{d}{d\sigma} H[\mathbf{x}_0 | \mathbf{x}_\sigma]. \quad (12)$$

In what follows, we abuse notation and let  $\dot{H}[\mathbf{x}_0 | \mathbf{x}_\sigma]$  denote the scheduling signal, i.e., the entropy-rate possibly after low-noise regularization (Section 3.3), which we normalize to obtain  $\rho$ :

$$\rho(\sigma) \triangleq \frac{\dot{H}[\mathbf{x}_0 | \mathbf{x}_\sigma]}{\int_{\sigma_{\min}}^{\sigma_{\max}} \dot{H}[\mathbf{x}_0 | \mathbf{x}_{\tilde{\sigma}}] d\tilde{\sigma}}, \quad \sigma \in [\sigma_{\min}, \sigma_{\max}], \quad (13)$$

and let  $u(\sigma)$  be its CDF,

$$u(\sigma) \triangleq \int_{\sigma_{\min}}^{\sigma} \rho(s) ds \in [0, 1]. \quad (14)$$

Sampling  $z \sim \mathcal{U}(0, 1)$  and setting  $\sigma = u^{-1}(z)$  draws  $\sigma$  with density  $\rho$  (inverse-CDF sampling). We call  $u$  *entropic time* (Stancevic et al., 2025). When  $\rho(\sigma) \propto \dot{H}[\mathbf{x}_0 | \mathbf{x}_\sigma]$ ,  $u$  equals the normalized conditional-entropy increase:

$$u(\sigma) = \frac{H[\mathbf{x}_0 | \mathbf{x}_\sigma] - H[\mathbf{x}_0 | \mathbf{x}_{\sigma_{\min}}]}{H[\mathbf{x}_0 | \mathbf{x}_{\sigma_{\max}}] - H[\mathbf{x}_0 | \mathbf{x}_{\sigma_{\min}}]} \in [0, 1]. \quad (15)$$

In practice, we tabulate  $u(\sigma)$  on a fixed  $\sigma$ -grid and evaluate  $u^{-1}$  by interpolation (Figure 3, left). Figure 3 illustrates the construction: the entropy-rate profile is normalized into  $\rho(\sigma)$  (left), and  $\rho$  is then translated into an implementable sampling schedule  $\pi(\sigma)$  after accounting for the training loss weight  $w(\sigma)$  (right).

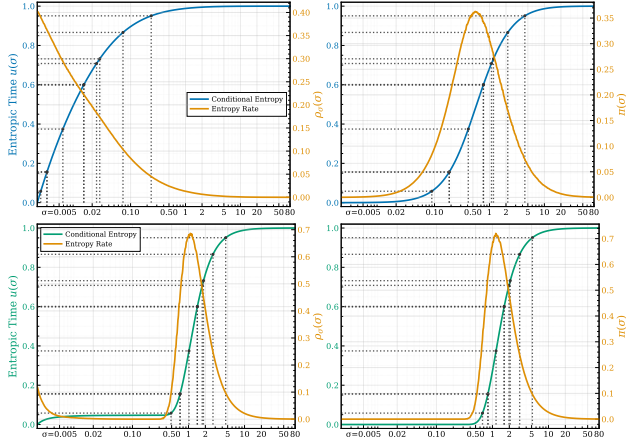


**Figure 3. INFOISE schedule construction (CIFAR-10, DNA).** **Left: from rate to allocation.** We estimate the entropy rate signal  $\dot{H}[\mathbf{x}_0 | \mathbf{x}_\sigma]$  and normalize it to a target density  $\rho(\sigma)$  (orange). Its CDF  $u(\sigma)$  defines *entropic time*: sampling uniformly in  $u$  concentrates draws in the  $\sigma$  ranges where uncertainty is reduced most rapidly. **Right: realizing  $\rho$  under weighted training.** With per-noise loss weights  $w(\sigma)$ , we sample  $\pi(\sigma) \propto \rho(\sigma)/w(\sigma)$  so that the effective emphasis  $\phi(\sigma) = \pi(\sigma)w(\sigma)$  matches  $\rho(\sigma)$  (up to normalization).

### 3.2. From a target allocation to a training schedule

In the weighted objective Equation (5), sampling  $\sigma \sim \pi(\sigma)$  and applying a fixed loss weight  $w(\sigma)$  induces an *effective emphasis*  $\phi(\sigma) \triangleq \pi(\sigma)w(\sigma)$  along the noise path. To make this emphasis follow the target allocation  $\rho(\sigma)$ , we set (assuming  $w(\sigma) > 0$  on  $[\sigma_{\min}, \sigma_{\max}]$ )

$$\pi(\sigma) \propto \frac{\rho(\sigma)}{w(\sigma)}. \quad (16)$$

Then  $\phi(\sigma) \propto \rho(\sigma)$ , increasing update frequency in the informative region while leaving the loss weighting of the underlying objective unchanged (Figure 3, right). When  $w(\sigma) \equiv 1$ , this simplifies to  $\pi(\sigma) = \rho(\sigma)$ .

### 3.3. Low-noise regularization of the scheduling signal

For continuous-valued data,  $H[\mathbf{x}_0 | \mathbf{x}_\sigma]$  is a differential entropy and its slope can exhibit a universal small-noise scaling as  $\sigma \rightarrow 0$ . After normalization, this can concentrate  $\rho$  near the low-noise boundary and mask the dataset-specific structure we want to track. We regularize the signal before normalization using the smooth gate

$$g_{c,n}(\sigma) \triangleq \frac{\sigma^n}{\sigma^n + c^n}, \quad c > 0, n \geq 2, \quad (17)$$

and form the pre-allocation  $\rho(\sigma) \propto \dot{H}[\mathbf{x}_0 | \mathbf{x}_\sigma] g_{c,n}(\sigma)$  before normalizing. The gate is near 1 for  $\sigma \gg c$  and decays smoothly for  $\sigma \ll c$ , suppressing only the extreme low-noise tail while leaving the mid-noise region essentially unchanged. Unless stated otherwise, we use  $n = 3$ .

For discrete endpoints,  $H[\mathbf{x}_0 | \mathbf{x}_\sigma]$  is bounded, but the entropy-rate in the  $\sigma$ -coordinate can still exhibit a strong low-noise scaling; empirically this regime is often well-approximated by a power law over several decades, which we exploit to set the boundary  $c$  (see Section 4 and Section B). We still apply the same gate to the estimated profile so that rare low- $\sigma$  spikes do not dominate  $\rho$ .

## 4. Automatic entropy gating calibration

The pivot  $c$  in Equation (17) sets where the low-noise gate transitions from suppression to the identity. We set  $c$  directly from the current online entropy-rate profile using a method that depends on the endpoint type. For **continuous endpoints**, we use an onset-of-information criterion. The profile is near-zero over much of the high-noise range and becomes appreciable only toward lower noise, so  $c$  marks where uncertainty reduction becomes substantial along the denoising direction. For **discrete endpoints**, the low-noise region typically exhibits an extended power-law regime in log-log scale (often visible as an approximately flat  $r(\sigma)\sigma$ ), so we set  $c$  at its departure; details are given in Section B.

**Onset-of-information rule (continuous endpoints).** Let  $r(\sigma) \triangleq \dot{H}[\mathbf{x}_0 | \mathbf{x}_\sigma]$  denote the current ungated entropy-rate profile estimated online (Section 5). We normalize by its peak,

$$\bar{r}(\sigma) \triangleq \frac{r(\sigma)}{\max_{\bar{\sigma}} r(\bar{\sigma})} \in [0, 1],$$

so that  $\bar{r} = 1$  marks the most information-dense regime. Scanning from high to low noise, we define the onset level as the first persistent crossing of a fixed threshold  $p \in (0, 1)$ :

$$c \triangleq \sup\{\sigma \mid \bar{r}(\sigma') < p \text{ for all } \sigma' \geq \sigma\}. \quad (18)$$

Thus  $c$  marks where the entropy-rate becomes appreciable along the denoising direction, and the gate is applied to the low-noise portion  $\sigma \leq c$ . We use  $p = 0.002$  throughout and recompute  $c$  whenever the schedule is updated. See Section B for more details.

## 5. INFOISE: Online schedule adaptation

Section 3 shows how the conditional-entropy rate  $r(\sigma) = \frac{d}{d\sigma} H[\mathbf{x}_0 | \mathbf{x}_\sigma]$  defines a target allocation and, after accounting for the training loss weight  $w(\sigma)$ , a schedule over noise levels. Since this profile depends on the Bayes MMSE via I-MMSE, it is not available when training from scratch. INFOISE estimates it online from the denoising losses already computed during SGD and periodically rebuilds a *continuous* sampler over  $\sigma$ . The diffusion objective is unchanged; only the sampling distribution over  $\sigma$  is adapted.

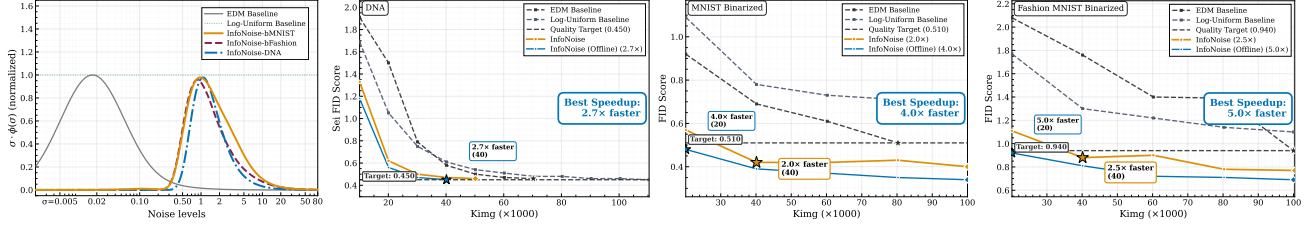


Figure 4. **Discrete domains expose schedule mismatch.** **Left:** Offline reference allocation (from a frozen checkpoint) versus the emphasis induced by fixed samplers (EDM log-normal, log-uniform) and by INFO NOISE. **Right:** Quality versus training compute on DNA (Sei FID) and binarized images (FID).

### Algorithm 1 INFO NOISE: Online schedule adaptation

**Require:** log-grid  $\{(\sigma_k, \Delta\sigma_k, I_k)\}_{k=1}^K$ , baseline sampler  $\pi_{\text{base}}$ , warm-up  $N_{\text{warm}}$ , refresh period  $M$ , FIFO capacity  $B$ , EMA rate  $\beta$ , loss weight  $w(\sigma)$ , gate exponent  $n_{\text{gate}}$ , minimum per-bin count  $N_{\text{min}}$

- 1: Init FIFO buffers  $\{\mathcal{B}_k\}_{k=1}^K$  (cap.  $B$ , evict oldest if full)
- 2: Init  $\widehat{\text{mse}}_k \leftarrow 0$  and  $n_k \leftarrow 0$  for  $k = 1, \dots, K$
- 3: Init sampler  $\hat{\pi} \leftarrow \pi_{\text{base}}$ , step  $s \leftarrow 0$
- 4: **repeat**
- 5:    $s \leftarrow s + 1$
- 6:   Sample  $\sigma \sim \pi_{\text{base}}$  if  $s \leq N_{\text{warm}}$ , else  $\sigma \sim \hat{\pi}$
- 7:   Compute  $\ell = \|\hat{\mathbf{x}}_0 - \mathbf{x}_0\|_2^2$  at  $\sigma$ ; SGD on  $w(\sigma)\ell$
- 8:   Find  $k$  with  $\sigma \in I_k$ ; push  $\ell$  to  $\mathcal{B}_k$ ;  $n_k \leftarrow \min(n_k + 1, B)$
- 9:   **if**  $s > N_{\text{warm}}$  **and**  $s \bmod M = 0$  **and**  $\min_j n_j \geq N_{\text{min}}$  **then**
- 10:      $\bar{\ell}_k \leftarrow \frac{1}{|\mathcal{B}_k|} \sum_{\ell \in \mathcal{B}_k} \ell$  for  $k = 1, \dots, K$
- 11:      $\widehat{\text{mse}}_k \leftarrow (1 - \beta)\widehat{\text{mse}}_k + \beta \bar{\ell}_k$  for  $k = 1, \dots, K$
- 12:      $\hat{r}_k \leftarrow \widehat{\text{mse}}_k / \sigma_k^3$  for  $k = 1, \dots, K$
- 13:     Calibrate pivot  $c$  from  $\{\hat{r}_k\}_{k=1}^K$
- 14:      $\tilde{r}_k \leftarrow \hat{r}_k g_{c, n_{\text{gate}}}(\sigma_k)$  for  $k = 1, \dots, K$
- 15:      $q_k \leftarrow \tilde{r}_k / w(\sigma_k)$  for  $k = 1, \dots, K$
- 16:      $\hat{\pi} \leftarrow \text{BUILDSAMPLER}(\{(\sigma_k, \Delta\sigma_k, q_k)\}_{k=1}^K)$
- 17:   **end if**
- 18: **until** training budget exhausted

**Online entropy-rate estimation.** Each SGD step produces a pair  $(\sigma, \ell)$  at a sampled (continuous) noise level, and the same loss  $\ell = \|\hat{\mathbf{x}}_0 - \mathbf{x}_0\|_2^2$  used for the SGD update is also used for scheduling. We route  $(\sigma, \ell)$  to its log-grid interval  $I_k$  and keep a FIFO buffer  $\mathcal{B}_k$  of recent losses per bin. At refresh time, we average the buffer to obtain  $\bar{\ell}_k$ , smooth  $\bar{\ell}_k$  across refreshes to obtain a stable per-bin loss estimate  $\widehat{\text{mse}}_k$ , and then form the entropy-rate estimate via I-MMSE (Equation 11),  $\hat{r}_k = \widehat{\text{mse}}_k / \sigma_k^3$ . The grid is used for estimation and numerical integration; sampling remains continuous.

**Boundary regularization and pivot calibration.** Raw estimates can concentrate near  $\sigma_{\text{min}}$  (Section 3.3). At each refresh, we set the pivot  $c$  from the current profile (power-law boundary for discrete endpoints; onset-of-information for continuous endpoints; see Sections B and 4), then apply the gate  $g_{c, n_{\text{gate}}}$  to suppress only the extreme low-noise tail. Optionally, we apply light smoothing across neighboring grid points on the log-grid to reduce estimator noise without

shifting the dominant peak. We denote the resulting (gated, optionally smoothed) profile by  $\tilde{r}_k$ .

**Sampler refresh and continuous realization.** Every  $M$  optimization steps, once all intervals have at least  $N_{\text{min}}$  samples, we rebuild the sampler. We convert the gated profile into tabulated density values  $q_k \propto \tilde{r}_k / w(\sigma_k)$  so that the effective emphasis  $\phi(\sigma) = \pi(\sigma)w(\sigma)$  follows Section 3. BUILDSAMPLER normalizes  $\{q_k\}$  using  $\Delta\sigma_k$ , builds a continuous CDF by numerical integration over  $\sigma$ , and samples continuous  $\sigma$  values via inverse-CDF interpolation.

**Warm-up and stability.** We use a fixed baseline sampler  $\pi_{\text{base}}$  for  $N_{\text{warm}}$  steps to populate all intervals. We also enforce a minimum count  $N_{\text{min}}$  before each refresh, preventing updates driven by under-sampled regions. The FIFO capacity  $B$  keeps the estimate responsive as the model changes, while the refresh period  $M$  controls how often the sampler is rebuilt.

## 6. Experiments

Noise schedules determine how training updates are distributed along the corruption path, and therefore which stages of uncertainty resolution receive compute. Our goal is to test whether allocating updates according to dataset-specific information dynamics improves training efficiency *without modifying the diffusion objective*.

We study four questions:

1. Do image-tuned schedules misallocate compute when transferred to discrete representations?
2. Can the informative region emerge *online* from the evolving denoiser?
3. Does entropy-rate adaptation remain competitive on mature image benchmarks with refined hand-tuned schedules?
4. Can the learned allocation also improve inference-time discretization at fixed NFE?

**Experimental setup.** Unless stated otherwise, we fix architecture, optimizer, augmentations, EMA, and training budget, and vary only the sampling distribution  $\pi(\sigma)$  (hence

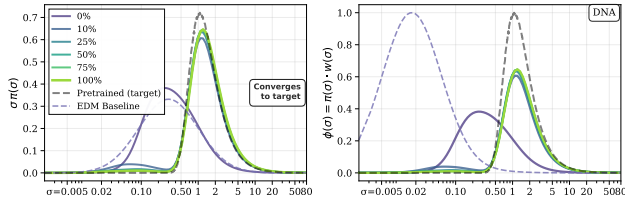


**Figure 5. Online schedule emergence on DNA.** Evolution of the training noise schedule  $\pi(\sigma)$  at several points during training (early→late), after an initial warm-up under  $\pi_{\text{base}}$ . The black curve shows the offline diagnostic computed from a frozen, converged checkpoint (analysis-only). INFO NOISE rapidly concentrates mass in a narrow intermediate-noise band and then changes little, indicating that the informative region is detectable early.

the realized emphasis  $\phi(\sigma) = \pi(\sigma)w(\sigma)$ . On continuous images, we keep the EDM objective fixed (including  $w_{\text{EDM}}(\sigma)$ ) and adapt only  $\pi(\sigma)$ . On discrete domains, primary comparisons use *allocation-controlled* training with  $w(\sigma) \equiv 1$ , so that  $\phi(\sigma) = \pi(\sigma)$  directly reflects compute allocation. We additionally report an *EDM transfer* baseline that applies the full EDM recipe (log-normal sampler and  $w_{\text{EDM}}$ ) without retuning.

**Compute and metrics.** We measure compute in thousands of processed examples (kEx) and report FID on images (Heusel et al., 2017) and Sei-FID on DNA (Chen et al., 2022).

**Compute-to-target.** Let  $m^*$  denote the best score achieved by any fixed baseline within the plotted budget. We report the first kEx at which each method reaches  $\leq m^*$ , or the budget limit if unattained.

**Offline diagnostics.** Offline diagnostics refer to entropy-rate profiles computed from a frozen, well-trained checkpoint and are used for analysis only. Implementation details are provided in Section D.

### 6.1. Transfer across representations

We begin with a controlled test of schedule transfer from continuous images to discrete representations. Figure 4 compares (i) an *EDM transfer* baseline (log-normal sampler +  $w_{\text{EDM}}$ ), (ii) a log-uniform sampler under  $w \equiv 1$ , and (iii) INFO NOISE under  $w \equiv 1$ . The left panel overlays the induced emphasis against the offline diagnostic allocation; the right panels report quality versus compute.

**Result.** Across all discrete datasets, the offline diagnostic concentrates mass in a narrow intermediate band, while fixed schedules allocate substantial compute outside this resolving region. INFO NOISE shifts probability mass toward the diagnostic band and reaches the best fixed baseline. Table 1(a) summarizes final quality and compute-to-target,

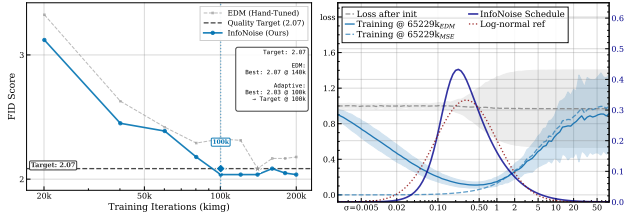


**Figure 6. Continuous images (EDM objective).** **Left:** Unconditional CIFAR-10 FID versus training compute with identical architecture, optimizer, and objective; only the sampler  $\pi(\sigma)$  is changed. **Right:** The resulting emphasis  $\phi(\sigma) = \pi(\sigma)w_{\text{EDM}}(\sigma)$  along the noise path. INFO NOISE concentrates updates in the same intermediate-noise band as EDM’s tuned schedule, while reaching the target FID earlier via small redistributions within that band.

yielding 1.5–2.8 $\times$  reductions in examples-to-target relative to the best fixed baseline.

We next visualize how this allocation emerges online on DNA sequence in Section 6.2.

### 6.2. Online emergence of the informative region

Starting from a short warm-up under a fixed sampler, INFO NOISE periodically refreshes  $\pi(\sigma)$  using only running denoising-error statistics. Figure 5 shows that the informative region emerges rapidly and settles early in training. The emphasis profile stabilizes well before final convergence, suggesting that the informative window is identifiable from intermediate dynamics rather than requiring a fully converged denoiser.

### 6.3. Competitive performance on image benchmarks

We evaluate continuous images while keeping the EDM objective fixed and varying only  $\pi(\sigma)$ .

**Unconditional training efficiency.** On unconditional CIFAR-10, INFO NOISE reaches the same FID target earlier than the hand-tuned EDM sampler (Figure 6, left), corresponding to a 1.4 $\times$  reduction in training compute. The learned emphasis concentrates in the same intermediate-noise window identified by EDM, with modest redistribution within that region (Figure 6, right). Although EDM’s schedule was obtained through extensive empirical tuning, INFO NOISE recovers the same band directly from online entropy-rate estimation, without manual schedule search. This agreement suggests that the intermediate-noise window reflects intrinsic information dynamics of the dataset rather than an artifact of heuristic tuning.

This pattern holds across continuous datasets: INFO NOISE matches or slightly improves MNIST and FashionMNIST under identical objectives with comparable or better efficiency, and remains competitive with the tuned EDM schedule on FFHQ 64 $\times$ 64 despite fully automatic adaptation (see Table 1(b)).

(a) Discrete domains (main: $w \equiv 1$ ; transfer: EDM recipe)								(b) Continuous images (EDM objective)				
Dataset	Final ↓			kEx@target ↓			Speedup	Dataset	Final FID ↓			Speedup
	log-unif	EDM	INFONOISE	log-unif	EDM	INFONOISE	×		log-unif	EDM	INFONOISE	×
bMNIST (FID)	0.63	0.53	0.40	100	80	40	2.0	MNIST	1.02	0.44	0.43	1.0
bFashionMNIST (FID)	1.10	0.94	0.89	100	100	40	2.5	FashionMNIST	2.75	1.78	1.71	1.0
DNA (Sei-FID)	0.61	0.45	0.42	100	100	40	2.7	CIFAR-10 (uncond.)	5.93	2.04	1.98	1.4
								CIFAR-10 (cond.)	4.45	1.85	1.84	1.5
								FFHQ 64×64	4.68	2.53	2.56	—

Table 1. **Training efficiency across domains.** (a) Discrete domains: final quality and compute-to-target (kEx) under  $w \equiv 1$  (log-unif, INFONOISE) plus an EDM transfer baseline (EDM sampler +  $w_{\text{EDM}}$ ). (b) Continuous images: final FID under the EDM objective; speedup reports the reduction in training compute to reach a fixed FID target (when measured). “kEx” denotes thousands of processed examples; targets follow Figure 4.

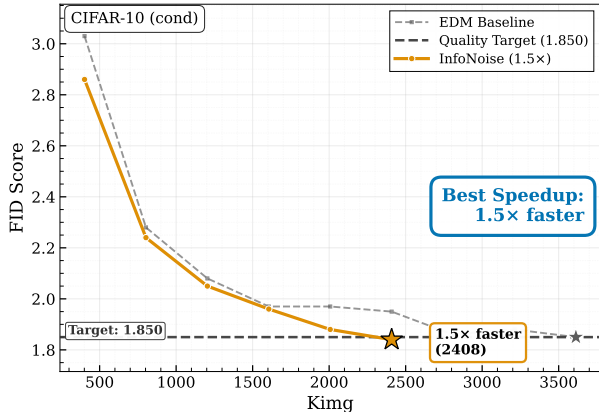


Figure 7. **Class-conditional CIFAR-10 training efficiency.** FID ( $\downarrow$ ) versus kimg under the same training recipe and objective, varying only  $\pi(\sigma)$ . INFONOISE reaches the EDM target with  $1.5\times$  fewer processed examples, showing that the efficiency gains persist under conditioning.

**Conditional training efficiency.** On class-conditional CIFAR-10, INFONOISE attains the same FID target as the EDM sampler with  $1.5\times$  fewer processed examples (Figure 7), indicating that the efficiency gains persist under conditioning.

#### 6.4. Information-guided discretization for inference

We next address question (iv): whether the information profile learned during training can also improve inference-time discretization at fixed compute. INFONOISE estimates an entropy-rate profile  $r(\sigma)$  along the corruption path, which captures where uncertainty about  $\mathbf{x}_0$  is resolved most rapidly as noise decreases. Integrating this profile induces a cumulative coordinate over noise levels, and uniform spacing in that coordinate yields a discretization that allocates solver evaluations proportionally to intrinsic information density.

**InfoGrid construction.** Given the learned entropy-rate profile  $r(\sigma)$  (Section 5), we define the normalized cumulative information coordinate

$$u(\sigma) \triangleq \frac{1}{Z} \int_{\sigma_{\min}}^{\sigma} \tilde{\sigma} r(\tilde{\sigma}) d\tilde{\sigma}, \quad Z = \int_{\sigma_{\min}}^{\sigma_{\max}} \tilde{\sigma} r(\tilde{\sigma}) d\tilde{\sigma}. \quad (19)$$

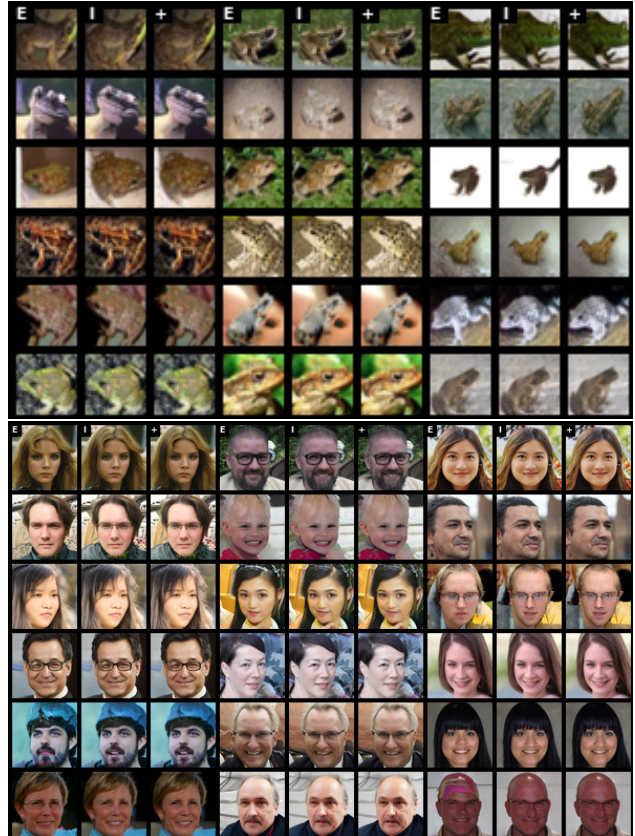


Figure 8. **Conditional CIFAR-10 and unconditional FFHQ samples.** All runs use the same architecture, objective, solver (Heun), and NFE (35, top; 79, bottom); only the *training schedule* and/or the *inference grid* differs. (E) EDM training with the standard EDM  $\sigma$ -grid. (I) INFONOISE training with the same EDM grid. (I+) INFONOISE training with an information-guided inference grid (InfoGrid) built from the learned  $u(\sigma)$ . INFONOISE yields cleaner samples; InfoGrid remains stable.

The extra factor  $\tilde{\sigma}$  matches the log-noise measure used in Section 3 (equivalently, it corresponds to working in the log-noise parameterization (Stancevic et al., 2025)). We then choose the inference grid by spacing points uniformly in  $u$  and mapping them back through  $u^{-1}$ . This yields a non-uniform grid in  $\sigma$  whose steps are (approximately) linear in information space, distributing solver evaluations where uncertainty is actually resolved (Figure 9(b,c)).

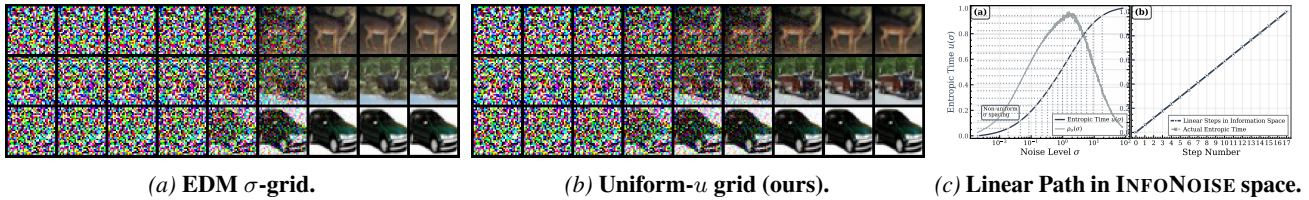


Figure 9. **Information-guided discretization for sampling.** Sample paths from the same initial noise, model, solver (Heun), and NFE. The only difference is the discretization of  $\sigma$ . (a) The default EDM grid allocates steps unevenly in information space, leading to late-stage noise removal. (b) Uniform spacing in the learned information coordinate produces more evenly distributed denoising progress. (c) The cumulative information map  $u(\sigma)$  underlying the grid construction.

We test this at fixed compute by replacing the hand-designed EDM  $\sigma$ -grid with InfoGrid. In all comparisons, the model checkpoint, objective, solver (Heun), and number of function evaluations (NFE) are held fixed; only the  $\sigma$  discretization changes. Figure 8 shows that replacing the EDM grid with InfoGrid yields consistently cleaner or comparable samples at equal NFE.

**Straight paths in the appropriate coordinate.** Straightness in  $\sigma$  does not imply uniform information resolution. Uniform spacing in the learned information coordinate instead produces a trajectory with more evenly distributed uncertainty reduction (Figure 9).

Taken together, these results show that the informative band can be identified online, improves training efficiency when schedules transfer poorly, remains competitive with tuned image schedules, and also yields an effective inference-time discretization at fixed NFE.

## 7. Related work

**Noise schedules.** The sensitivity of diffusion models to the noise schedule was recognized early in nonequilibrium formulations of generative diffusion (Sohl-Dickstein et al., 2015). Early implementations relied on hand-crafted, monotone noise-level parameterizations (e.g., linear variance schedules or log-spaced noise scales) (Ho et al., 2020; Song & Ermon, 2019). Later work showed that performance depends on how optimization effort is distributed along the corruption path, motivating shaped schedules (e.g., cosine) and SNR-aware weighting (Nichol & Dhariwal, 2021; Kingma et al., 2021; Kingma & Gao, 2023). A consistent empirical finding is that useful learning signal concentrates in an intermediate noise region: at very high noise, structure is obscured, whereas at very low noise, marginal gains diminish; many heuristics can be read as different ways of emphasizing this regime (cosine/SNR-based weighting, clipping, or logSNR shifts) (Hang et al., 2023; Hoogeboom et al., 2023; Chen, 2023). EDM makes this allocation explicit via a parametric log-normal sampler over  $\sigma$  (Karras et al., 2022), yet scaling and representation changes require retuning its sampler parameters, suggesting that the infor-

mative window is representation-dependent (Karras et al., 2024). Related work studies transfer across settings (Teng et al., 2023). Separately, inference-time grids can be designed by controlling discretization error in reverse-time dynamics (de Bortoli et al., 2025). Flow matching (Lipman et al., 2023) and rectified-flow scaling (Esser et al., 2024) likewise rely on time parameterizations and weightings that determine where learning concentrates, and these choices are typically tuned. In contrast, we cast schedule choice as noise-level allocation and use the conditional entropy-rate to track denoising difficulty in a data-dependent way, guiding allocation during training toward the informative region.

**Information theory and diffusion models.** For Gaussian corruption, I-MMSE (Guo et al., 2005) links conditional entropy (and its rate along the noise axis) to Bayes-optimal denoising error, enabling a per-noise notion of denoising difficulty. This bridge has supported likelihood-related estimators and information-theoretic analyses (Kong et al., 2023; Franzese et al., 2024), as well as information-based regularization objectives (Wang et al., 2023; Premkumar, 2025; Wang et al., 2025). Closest in spirit, entropy-rate signals have been used to reparameterize time so that equal steps correspond to approximately equal information change along the path (Stancevic et al., 2025; Ambrogioni, 2025). However, these uses are primarily analytical, representational, or inference-time. To our knowledge, prior work has not used the I-MMSE/entropy-rate link as an online training-time control signal to adapt the noise sampling distribution while leaving the underlying objective unchanged.

**Diffusion beyond continuous images.** Outside continuous images, corruption geometry and representation shift, so image-tuned schedules need not transfer. For categorical data, Dieleman et al. (2022) learn a monotone time warp from loss-noise statistics and use inverse-CDF sampling to reshape the training noise distribution; for discrete diffusion, Amin et al. (2025) conditions the reverse model on the jump-time schedule. INFONoise addresses this by estimating an entropy-rate profile online and reallocating sampling mass accordingly, avoiding hand-designed schedules that assume transfer across representations.

## 8. Discussion and conclusions

We introduced INFOISE, an adaptive noise scheduler that reallocates training updates toward noise levels where uncertainty about the clean sample is reduced most rapidly. The construction follows from the I-MMSE relation for additive Gaussian corruption, which links the slope of the conditional entropy  $H[x_0 | x_\sigma]$  to the Bayes-optimal denoising error along the noise path. This yields a dataset- and representation-dependent profile over  $\sigma$  that can be used as a direct allocation signal. This perspective also explains why hand-tuned schedules can be brittle. A schedule tuned on a particular dataset or representation implicitly targets a specific uncertainty-removal geometry along  $\sigma$ . When that geometry shifts, the same  $\sigma$  values correspond to a different amount of remaining ambiguity, so updates can be spent in regions that resolve little uncertainty. Our experiments make this mismatch visible when schedules tuned for continuous images are transferred to discrete representations, and show that INFOISE instead tracks the informative region online without retuning. On image benchmarks where existing schedules are already strong, INFOISE matches sample quality and can improve training efficiency under the same objective. The same learned information profile can also be reused at inference time to construct grids that take approximately uniform steps in information space, improving discretization at fixed NFE.

**Limitations.** INFOISE relies on online, model-dependent estimates of the entropy-rate profile derived from denoising losses, so the signal can be high-variance early in training. In practice, warm-up and low-noise regularization mainly serve to prevent transient misallocation of samples (e.g., brief over-emphasis near  $\sigma_{\min}$ ), which can waste a small amount of compute rather than affect convergence. The method also introduces a few scheduler settings (e.g., refresh cadence, buffer/averaging horizon, and gating calibration) that control how quickly the allocation reacts to new evidence versus averaging out noise.

**Future work.** For continuous data, a key direction is more principled regularization of the low-noise regime that avoids degenerate over-allocation while preserving the informative band. More broadly, the information-allocation view suggests a path toward characterizing schedules that are optimal for a given objective and compute budget, and toward online methods that can track such schedules reliably as training evolves. Extending the same principles beyond Gaussian corruption, and tightening the connection between loss-derived signals and uncertainty reduction in non-Gaussian or discrete mechanisms, are also important directions.

## Acknowledgements

This work was supported by the Dutch Research Council (NWO) as part of the CERTIF-AI project (file number 17998).

## Impact Statement

This paper advances the methodological foundations of diffusion training by replacing hand-tuned noise schedules with a data-adaptive allocation principle grounded in information dynamics along the corruption path. By reducing trial-and-error schedule design, our approach can lower the compute and engineering burden of deploying diffusion models across new datasets, resolutions, and representations, potentially accelerating research and broadening access. At the same time, improved efficiency can lower the marginal cost of generating high-fidelity synthetic data, amplifying both beneficial uses and harmful misuse.

## References

- Ambrogioni, L. The information dynamics of generative diffusion. *arXiv preprint arXiv:2508.19897*, 2025.
- Amin, A. N., Gruver, N., and Wilson, A. G. Why masking diffusion works: Condition on the jump schedule for improved discrete diffusion. *arXiv preprint arXiv:2506.08316*, 2025.
- Anderson, B. D. Reverse-time diffusion equation models. *Stochastic Processes and their Applications*, 12(3):313–326, 1982.
- Austin, J., Johnson, D. D., Ho, J., Tarlow, D., and Van Den Berg, R. Structured denoising diffusion models in discrete state-spaces. *Advances in neural information processing systems*, 34:17981–17993, 2021.
- Biroli, G., Bonnaire, T., De Bortoli, V., and Mézard, M. Dynamical regimes of diffusion models. *Nature Communications*, 15(1):9957, 2024.
- Chen, K. M., Wong, A. K., Troyanskaya, O. G., and Zhou, J. A sequence-based global map of regulatory activity for deciphering human genetics. *Nature genetics*, 54(7):940–949, 2022.
- Chen, T. On the importance of noise scheduling for diffusion models. *arXiv preprint arXiv:2301.10972*, 2023.
- Collier, J. Information originates in symmetry breaking. *Symmetry: Culture & Science*, 7(1996):247–256, 1996.
- DaSilva, L. F., Senan, S., Patel, Z. M., Reddy, A. J., Gabbita, S., Nussbaum, Z., Córdova, C. M. V., Wenteler, A., Weber, N., Tunjic, T. M., et al. Dna-diffusion: leveraging

- generative models for controlling chromatin accessibility and gene expression via synthetic regulatory elements. *Biorxiv*, 2024.
- de Bortoli, V., Elie, R., Kazeykina, A., Ren, Z., and Zhang, J. Dimension-free error estimate for diffusion model and optimal scheduling. *arXiv preprint arXiv:2512.01820*, 2025.
- Dieleman, S., Sartran, L., Roshannai, A., Savinov, N., Ganin, Y., Richemond, P. H., Doucet, A., Strudel, R., Dyer, C., Durkan, C., et al. Continuous diffusion for categorical data. *arXiv preprint arXiv:2211.15089*, 2022.
- Esser, P., Kulal, S., Blattmann, A., Entezari, R., Müller, J., Saini, H., Levi, Y., Lorenz, D., Sauer, A., Boesel, F., et al. Scaling rectified flow transformers for high-resolution image synthesis. In *Forty-first international conference on machine learning*, 2024.
- Franzese, G., Bounoua, M., and Michiardi, P. MINDE: Mutual information neural diffusion estimation. In *The Twelfth International Conference on Learning Representations*, 2024. URL <https://openreview.net/forum?id=0kWd8SJq8d>.
- Guo, D., Shamai, S., and Verdú, S. Mutual information and minimum mean-square error in gaussian channels. *IEEE transactions on information theory*, 51(4):1261–1282, 2005.
- Hang, T., Gu, S., Li, C., Bao, J., Chen, D., Hu, H., Geng, X., and Guo, B. Efficient diffusion training via min-snr weighting strategy. In *Proceedings of the IEEE/CVF international conference on computer vision*, pp. 7441–7451, 2023.
- Heusel, M., Ramsauer, H., Unterthiner, T., Nessler, B., and Hochreiter, S. Gans trained by a two time-scale update rule converge to a local nash equilibrium. *Advances in neural information processing systems*, 30, 2017.
- Ho, J., Jain, A., and Abbeel, P. Denoising diffusion probabilistic models. *Advances in Neural Information Processing Systems*, 2020.
- Hoogeboom, E., Heek, J., and Salimans, T. simple diffusion: End-to-end diffusion for high resolution images. In *International Conference on Machine Learning*, pp. 13213–13232. PMLR, 2023.
- Karras, T., Aittala, M., Aila, T., and Laine, S. Elucidating the design space of diffusion-based generative models. *Advances in neural information processing systems*, 35: 26565–26577, 2022.
- Karras, T., Aittala, M., Lehtinen, J., Hellsten, J., Aila, T., and Laine, S. Analyzing and improving the training dynamics of diffusion models. In *Proceedings of the IEEE/CVF Conference on Computer Vision and Pattern Recognition*, pp. 24174–24184, 2024.
- Kingma, D. and Gao, R. Understanding diffusion objectives as the elbo with simple data augmentation. *Advances in Neural Information Processing Systems*, 36:65484–65516, 2023.
- Kingma, D., Salimans, T., Poole, B., and Ho, J. Variational diffusion models. *Advances in neural information processing systems*, 34:21696–21707, 2021.
- Kong, X., Brekelmans, R., and Steeg, G. V. Information-theoretic diffusion. In *The Eleventh International Conference on Learning Representations*, 2023. URL <https://openreview.net/forum?id=UvmDCdSPDOW>.
- Lai, C.-H., Song, Y., Kim, D., Mitsufuji, Y., and Ermon, S. The principles of diffusion models. *arXiv preprint arXiv:2510.21890*, 2025.
- Lee, S., Lee, K., and Park, T. Ant: Adaptive noise schedule for time series diffusion models. *Advances in Neural Information Processing Systems*, 37:121099–121130, 2024.
- Lehmann, E. L. and Casella, G. *Theory of point estimation*. Springer, 1998.
- Li, M. and Chen, S. Critical windows: non-asymptotic theory for feature emergence in diffusion models. *arXiv preprint arXiv:2403.01633*, 2024.
- Lipman, Y., Chen, R. T. Q., Ben-Hamu, H., Nickel, M., and Le, M. Flow matching for generative modeling. In *The Eleventh International Conference on Learning Representations*, 2023. URL <https://openreview.net/forum?id=PqvMRDCJT9t>.
- Nichol, A. Q. and Dhariwal, P. Improved denoising diffusion probabilistic models. In *International conference on machine learning*, pp. 8162–8171. PMLR, 2021.
- Palomar, D. P. and Verdú, S. Gradient of mutual information in linear vector gaussian channels. *IEEE Transactions on Information Theory*, 52(1):141–154, 2005.
- Premkumar, A. Neural entropy. In *The Thirty-ninth Annual Conference on Neural Information Processing Systems*, 2025. URL <https://openreview.net/forum?id=f6AYwCvynr>.
- Raya, G. and Ambrogioni, L. Spontaneous symmetry breaking in generative diffusion models. *Advances in Neural Information Processing Systems*, 36, 2024.
- Sinha, S. and Kooloth, P. On information transfer and symmetry breaking in dynamical systems. *arXiv e-prints*, pp. arXiv–2510, 2025.

- Sohl-Dickstein, J., Weiss, E., Maheswaranathan, N., and Ganguli, S. Deep unsupervised learning using nonequilibrium thermodynamics. In *International Conference on Machine Learning*, 2015.
- Song, Y. and Ermon, S. Generative modeling by estimating gradients of the data distribution. *Advances in neural information processing systems*, 32, 2019.
- Song, Y., Sohl-Dickstein, J., Kingma, D. P., Kumar, A., Ermon, S., and Poole, B. Score-based generative modeling through stochastic differential equations. *arXiv preprint arXiv:2011.13456*, 2020.
- Stancevic, D., Handke, F., and Ambrogioni, L. Entropic time schedulers for generative diffusion models. *arXiv preprint arXiv:2504.13612*, 2025.
- Teng, J., Zheng, W., Ding, M., Hong, W., Wangni, J., Yang, Z., and Tang, J. Relay diffusion: Unifying diffusion process across resolutions for image synthesis. *arXiv preprint arXiv:2309.03350*, 2023.
- Wang, C., Franzese, G., Finamore, A., Gallo, M., and Michiardi, P. Information theoretic text-to-image alignment. In *International Conference on Learning Representations*, 2025. URL <https://openreview.net/forum?id=Ugs2W5XFFo>.
- Wang, Y., Schiff, Y., Gokaslan, A., Pan, W., Wang, F., De Sa, C., and Kuleshov, V. InfoDiffusion: Representation learning using information maximizing diffusion models. In Krause, A., Brunskill, E., Cho, K., Engelhardt, B., Sabato, S., and Scarlett, J. (eds.), *Proceedings of the 40th International Conference on Machine Learning*, volume 202 of *Proceedings of Machine Learning Research*, pp. 36336–36354. PMLR, 23–29 Jul 2023. URL <https://proceedings.mlr.press/v202/wang23ah.html>.

# Appendix

## A. Conditional-entropy rates and I-MMSE

INFONOISE relies on the I-MMSE identity for the additive Gaussian channel (Guo et al., 2005), which links Bayes-optimal denoising error to how conditional uncertainty changes along the noise axis. In particular, the Bayes MMSE  $\text{mmse}(\sigma)$  equals the expected posterior uncertainty under squared loss, and therefore quantifies the irreducible denoising difficulty at noise level  $\sigma$ . For the variance-exploding channel  $x_\sigma = x_0 + \sigma\epsilon$ , this uncertainty controls the conditional-entropy rate:  $\frac{d}{d\sigma} H[\mathbf{x}_0 | \mathbf{x}_\sigma] = \text{mmse}(\sigma)/\sigma^3$ . We also analyze a one-dimensional symmetric toy distribution to show explicitly how posterior concentration with decreasing  $\sigma$  yields the ‘‘information window’’ behavior described in the main text.

### A.1. Gaussian channel, Bayes MMSE, and entropy-rate

**Channel and induced marginals.** Consider the variance-exploding Gaussian channel

$$\mathbf{x}_\sigma = \mathbf{x}_0 + \sigma \boldsymbol{\epsilon}, \quad \mathbf{x}_0 \sim p_{\text{data}}, \quad \boldsymbol{\epsilon} \sim \mathcal{N}(\mathbf{0}, \mathbf{I}_d), \quad (20)$$

with  $\boldsymbol{\epsilon}$  independent of  $\mathbf{x}_0$ . The forward kernel is  $p_\sigma(\mathbf{x}_\sigma | \mathbf{x}_0) = \mathcal{N}(\mathbf{x}_\sigma; \mathbf{x}_0, \sigma^2 \mathbf{I}_d)$ , which induces the noisy marginal

$$p(\mathbf{x}_\sigma; \sigma) \triangleq \int p_{\text{data}}(\mathbf{x}_0) p_\sigma(\mathbf{x}_\sigma | \mathbf{x}_0) d\mathbf{x}_0, \quad (21)$$

and the posterior  $p(\mathbf{x}_0 | \mathbf{x}_\sigma; \sigma) \propto p_{\text{data}}(\mathbf{x}_0) p_\sigma(\mathbf{x}_\sigma | \mathbf{x}_0)$ .

**Bayes denoiser and MMSE (irreducible denoising difficulty).** The Bayes-optimal denoiser under squared loss is the posterior mean

$$\hat{\mathbf{x}}^*(\mathbf{x}_\sigma; \sigma) \triangleq \mathbb{E}[\mathbf{x}_0 | \mathbf{x}_\sigma; \sigma]. \quad (22)$$

For any estimator  $\hat{\mathbf{x}}(\mathbf{x}_\sigma)$  (measurable in  $\mathbf{x}_\sigma$ ),

$$\mathbb{E}[\|\mathbf{x}_0 - \hat{\mathbf{x}}(\mathbf{x}_\sigma)\|_2^2] \geq \mathbb{E}[\|\mathbf{x}_0 - \hat{\mathbf{x}}^*(\mathbf{x}_\sigma; \sigma)\|_2^2] =: \text{mmse}(\sigma), \quad (23)$$

so  $\text{mmse}(\sigma)$  is the *irreducible* (Bayes) denoising error at noise level  $\sigma$ . Equivalently, letting  $\Sigma(\mathbf{x}_\sigma; \sigma) \triangleq \text{Cov}(\mathbf{x}_0 | \mathbf{x}_\sigma; \sigma)$ ,

$$\text{mmse}(\sigma) = \mathbb{E}_{p(\mathbf{x}_\sigma; \sigma)}[\text{tr}(\Sigma(\mathbf{x}_\sigma; \sigma))]. \quad (24)$$

**I-MMSE and conditional-entropy rates.** Let  $\gamma \triangleq \sigma^{-2}$  and define the standardized observation

$$\tilde{\mathbf{x}}_\gamma \triangleq \frac{\mathbf{x}_\sigma}{\sigma} = \sqrt{\gamma} \mathbf{x}_0 + \boldsymbol{\epsilon}. \quad (25)$$

For fixed  $\sigma$ , the map  $\mathbf{x}_\sigma \leftrightarrow \tilde{\mathbf{x}}_\gamma$  is bijective, hence  $I(\mathbf{x}_0; \mathbf{x}_\sigma) = I(\mathbf{x}_0; \tilde{\mathbf{x}}_\gamma)$  and  $\mathbb{E}[\mathbf{x}_0 | \mathbf{x}_\sigma; \sigma] = \mathbb{E}[\mathbf{x}_0 | \tilde{\mathbf{x}}_\gamma]$ . Define  $\text{mmse}(\gamma) \triangleq \mathbb{E}[\|\mathbf{x}_0 - \mathbb{E}[\mathbf{x}_0 | \tilde{\mathbf{x}}_\gamma]\|_2^2]$ , so  $\text{mmse}(\sigma) = \text{mmse}(\gamma = \sigma^{-2})$ . The I-MMSE identity (Guo et al., 2005) states

$$\frac{\partial}{\partial \gamma} I(\mathbf{x}_0; \tilde{\mathbf{x}}_\gamma) = \frac{1}{2} \text{mmse}(\gamma). \quad (26)$$

Using  $H[\mathbf{x}_0 | \mathbf{x}_\sigma] = H[\mathbf{x}_0] - I(\mathbf{x}_0; \mathbf{x}_\sigma)$  and  $\gamma = \sigma^{-2}$  yields

$$\frac{d}{d\sigma} H[\mathbf{x}_0 | \mathbf{x}_\sigma] = \frac{\text{mmse}(\sigma)}{\sigma^3} \geq 0. \quad (27)$$

Equivalently, with log-SNR  $\lambda \triangleq \log \gamma = \log(1/\sigma^2)$ ,

$$-\frac{d}{d\lambda} H[\mathbf{x}_0 | \mathbf{x}_\sigma] = \frac{1}{2} \gamma \text{mmse}(\gamma) = \frac{1}{2} \frac{1}{\sigma^2} \text{mmse}(\sigma). \quad (28)$$

## A.2. Empirical Bayes formulas for a finite dataset

**Empirical prior and noisy marginal.** Given  $\{x_i\}_{i=1}^N \subset \mathbb{R}^d$ , define the empirical prior

$$p_{\text{data}}(x_0) = \frac{1}{N} \sum_{i=1}^N \delta(x_0 - x_i). \quad (29)$$

The marginal under (20) is the Gaussian mixture

$$p(x; \sigma) = \frac{1}{N} \sum_{i=1}^N \mathcal{N}(x; x_i, \sigma^2 \mathbf{I}_d). \quad (30)$$

Here and below  $x \in \mathbb{R}^d$  denotes an observation (a realization of  $\mathbf{x}_\sigma$ ).

**Posterior weights and Bayes denoiser.** Bayes' rule gives a posterior supported on  $\{x_i\}$ :

$$p(x_0 | \mathbf{x}_\sigma = x; \sigma) = \sum_{i=1}^N w_i(x; \sigma) \delta(x_0 - x_i),$$

with weights

$$w_i(x; \sigma) \triangleq p(\mathbf{x}_0 = x_i | \mathbf{x}_\sigma = x; \sigma) = \frac{\mathcal{N}(x; x_i, \sigma^2 \mathbf{I}_d)}{\sum_{j=1}^N \mathcal{N}(x; x_j, \sigma^2 \mathbf{I}_d)}, \quad \sum_{i=1}^N w_i(x; \sigma) = 1. \quad (31)$$

The Bayes denoiser is the posterior mean

$$\hat{\mathbf{x}}^*(x; \sigma) = \mathbb{E}[\mathbf{x}_0 | \mathbf{x}_\sigma = x; \sigma] = \sum_{i=1}^N w_i(x; \sigma) x_i. \quad (32)$$

Computing  $\hat{\mathbf{x}}^*(x; \sigma)$  amounts to evaluating the  $N$  posterior weights  $w_i(x; \sigma)$ , making the ideal denoiser tractable on small datasets (or subsets) and an exact reference under the empirical distribution. As  $\sigma$  decreases, the weights typically sharpen: at high noise they are diffuse (the estimate averages many plausible candidates), while at low noise they concentrate on a single exemplar (the estimate becomes nearly decisive). On CIFAR-10, this produces a rapid qualitative shift over an intermediate  $\sigma$  range rather than a uniform progression across the noise axis; see Figure 1 and the additional examples in Figure 12. See Section D.1 for the implementation details.

**Posterior covariance and MMSE.** The posterior covariance admits the explicit form

$$\text{Cov}(\mathbf{x}_0 | \mathbf{x}_\sigma = x; \sigma) = \sum_{i=1}^N w_i(x; \sigma) (x_i - \hat{\mathbf{x}}^*(x; \sigma))(x_i - \hat{\mathbf{x}}^*(x; \sigma))^\top, \quad (33)$$

and its trace equals the conditional MSE:

$$\text{tr Cov}(\mathbf{x}_0 | \mathbf{x}_\sigma = x; \sigma) = \sum_{i=1}^N w_i(x; \sigma) \|x_i - \hat{\mathbf{x}}^*(x; \sigma)\|_2^2. \quad (34)$$

Averaging (34) over  $x \sim p(x; \sigma)$  recovers  $\text{mmse}(\sigma)$  in (24), and thus the entropy rate (27).

**Log-density, score, and stationary points.** Up to an additive constant independent of  $x$ ,

$$\log p(x; \sigma) = -\frac{d}{2} \log(2\pi\sigma^2) + \log \left( \frac{1}{N} \sum_{i=1}^N \exp \left( -\frac{\|x - x_i\|_2^2}{2\sigma^2} \right) \right). \quad (35)$$

Differentiating yields the score. Writing  $\nabla_x \log p = \nabla_x p/p$  and differentiating each Gaussian term gives

$$\nabla_x \log p(x; \sigma) = \frac{1}{\sigma^2} \left( \sum_{i=1}^N w_i(x; \sigma) x_i - x \right) = \frac{\hat{\mathbf{x}}^*(x; \sigma) - x}{\sigma^2}, \quad (36)$$

which is the score–denoiser identity (Tweedie’s formula) specialized to the empirical prior. Therefore the stationary points of  $\log p(\cdot; \sigma)$  (equivalently, zeros of the score) satisfy the self-consistency equation

$$\nabla_x \log p(x; \sigma) = 0 \iff x = \hat{\mathbf{x}}^*(x; \sigma) = \sum_{i=1}^N w_i(x; \sigma) x_i. \quad (37)$$

**Local stability (optional).** A stationary point  $x^*$  is a local maximum of  $\log p(\cdot; \sigma)$  iff  $\nabla_x^2 \log p(x^*; \sigma)$  is negative definite (in  $d=1$ :  $\frac{\partial^2}{\partial x^2} \log p(x^*; \sigma) < 0$ ). For the Gaussian channel, differentiating (36) yields

$$\nabla_x^2 \log p(x; \sigma) = \frac{1}{\sigma^4} \text{Cov}(\mathbf{x}_0 \mid \mathbf{x}_\sigma = x; \sigma) - \frac{1}{\sigma^2} \mathbf{I}_d, \quad (38)$$

so local maxima require the posterior spread to be small compared to  $\sigma^2$ . We make this explicit in the one-dimensional toy model below.

### A.3. Symmetry breaking in a one-dimensional diffusion model

**Setup.** Following (Raya & Ambrogioni, 2024), we use a one-dimensional toy model to make symmetry breaking analytically transparent. In this setting, the conditional entropy rate provides a direct diagnostic for where posterior uncertainty collapses.

Let  $d = 1$  and consider the symmetric two-point data distribution

$$p_{\text{data}}(x_0) = \frac{1}{2} \delta(x_0 - a) + \frac{1}{2} \delta(x_0 + a), \quad a > 0, \quad (39)$$

which induces the marginal

$$p(x; \sigma) = \frac{1}{2} \mathcal{N}(x; a, \sigma^2) + \frac{1}{2} \mathcal{N}(x; -a, \sigma^2). \quad (40)$$

Figure 10 visualizes the induced marginal and the corresponding Bayes denoising field, highlighting the intermediate “decision window” where uncertainty collapses. Figure 10 visualizes the induced marginal  $p(x; \sigma)$ , the Bayes denoising field  $\hat{x}^*(x; \sigma)$ , and the corresponding posterior uncertainty via  $\text{mmse}(\sigma)$ , highlighting the intermediate region where uncertainty collapses.

#### Posterior weights, denoiser, and posterior variance.

The posterior weight on  $+a$  is

$$w_+(x; \sigma) = \frac{\mathcal{N}(x; a, \sigma^2)}{\mathcal{N}(x; a, \sigma^2) + \mathcal{N}(x; -a, \sigma^2)} = \frac{1}{1 + \exp\left(-\frac{2ax}{\sigma^2}\right)}, \quad w_-(x; \sigma) = 1 - w_+(x; \sigma), \quad (41)$$

so the Bayes denoiser is

$$\hat{x}^*(x; \sigma) = \mathbb{E}[x_0 \mid \mathbf{x}_\sigma = x; \sigma] = a(w_+(x; \sigma) - w_-(x; \sigma)) = a \tanh\left(\frac{ax}{\sigma^2}\right). \quad (42)$$

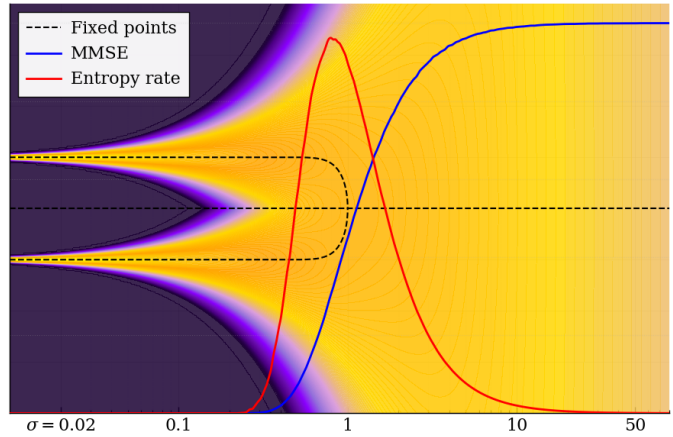


Figure 10. To complement Figure 1 (top), we plot the Bayes MMSE  $\text{mmse}(\sigma) = \mathbb{E}[\text{Var}(x_0 \mid x_\sigma; \sigma)]$ , which quantifies residual posterior uncertainty and irreducible denoising difficulty. Via I-MMSE,  $\text{mmse}(\sigma)$  sets  $\frac{d}{d\sigma} \mathbb{H}[x_0 \mid x_\sigma] = \text{mmse}(\sigma)/\sigma^3$ . The fixed-point branches reveal the symmetry-breaking transition. The peak in the entropy-rate aligns with this transition, where posterior mass concentrates and information is resolved. Plateaus in the entropy-rate indicate regimes where conditional uncertainty changes little, so samples there resolve minimal new information.

Since  $x_0 \in \{\pm a\}$ , the posterior variance is

$$\text{Var}(x_0 \mid \mathbf{x}_\sigma = x; \sigma) = a^2 - \hat{x}^*(x; \sigma)^2 = a^2 \operatorname{sech}^2\left(\frac{ax}{\sigma^2}\right), \quad (43)$$

hence  $\text{mmse}(\sigma) = \mathbb{E}_{x \sim p(\cdot; \sigma)}[\text{Var}(x_0 \mid \mathbf{x}_\sigma = x; \sigma)]$ , and the entropy-rate follows from (27).

**Score, self-consistency, and the critical noise region.** Using (36), the one-dimensional score takes the form

$$\frac{\partial}{\partial x} \log p(x; \sigma) = \frac{\hat{x}^*(x; \sigma) - x}{\sigma^2} = \frac{a \tanh\left(\frac{ax}{\sigma^2}\right) - x}{\sigma^2}. \quad (44)$$

The zeros of (44) are the stationary points of  $\log p(\cdot; \sigma)$  (equivalently, states of vanishing drift), and they organize the transition from a single symmetric attractor at high noise to two stable branches at lower noise (cf. Figure 10). Since (44) vanishes iff  $x = \hat{x}^*(x; \sigma)$ , these stationary points satisfy the self-consistency equation

$$x = \hat{x}^*(x; \sigma) \iff x = a \tanh\left(\frac{ax}{\sigma^2}\right). \quad (45)$$

The origin is always a solution. Linearizing  $\tanh(z) \approx z$  near 0 shows that the right-hand side has slope  $a^2/\sigma^2$  at the origin, so additional nonzero solutions appear when this slope exceeds 1, i.e.,

$$\frac{a^2}{\sigma^2} > 1 \iff \sigma < \sigma_c \triangleq a. \quad (46)$$

This corresponds to a stability change at  $x = 0$ . Using (38) at  $x = 0$  yields

$$\frac{\partial^2}{\partial x^2} \log p(0; \sigma) = \frac{a^2 - \sigma^2}{\sigma^4}, \quad (47)$$

so  $x = 0$  is a local maximum of  $\log p(x; \sigma)$  (stable for the score flow) when  $\sigma > \sigma_c$ , and a local minimum (unstable) when  $\sigma < \sigma_c$ . Thus  $p(x; \sigma)$  is unimodal for  $\sigma > \sigma_c$  and becomes bimodal for  $\sigma < \sigma_c$ , with two symmetric stable equilibria  $\pm x^*(\sigma)$  emerging via a pitchfork bifurcation. In energy terms, the potential  $U(x) = -\log p(x; \sigma)$  transitions from a single well to a double well as  $\sigma$  crosses  $\sigma_c$ , matching the “decision window” seen in Figure 1.

## B. Regularization of entropy-rate profiles and pivot selection

### B.1. Boundary structure of entropy-rate profiles

Entropy-rate profiles exhibit structured behavior near  $\sigma_{\min}$  for both endpoint types. After normalization, this boundary structure can disproportionately amplify the lowest log-decades relative to the interior, destabilizing allocation (see Figure 11).

**Continuous endpoints.** For continuous data,  $H[\mathbf{x}_0 \mid \mathbf{x}_\sigma]$  is a differential entropy and therefore unbounded below. As  $\sigma \rightarrow 0$ , the posterior  $p(\mathbf{x}_0 \mid \mathbf{x}_\sigma)$  concentrates with covariance of order  $\sigma^2$ . Consequently,

$$H[\mathbf{x}_0 \mid \mathbf{x}_\sigma] \asymp d \log \sigma \rightarrow -\infty,$$

up to additive constants that do not affect the slope.

Under standard regularity conditions, the Bayes error satisfies  $\text{mmse}(\sigma) = \Theta(\sigma^2)$ . Using the entropy–MMSE identity,

$$\frac{d}{d\sigma} H[\mathbf{x}_0 \mid \mathbf{x}_\sigma] = \frac{\text{mmse}(\sigma)}{\sigma^3},$$

we obtain the small-noise scaling

$$\frac{d}{d\sigma} H[\mathbf{x}_0 \mid \mathbf{x}_\sigma] = \Theta(\sigma^{-1}) \quad (\sigma \rightarrow 0). \quad (48)$$

Although integrable on any fixed interval  $[\sigma_{\min}, \sigma_{\max}]$ , this  $\sigma^{-1}$  behavior causes normalization to concentrate mass near  $\sigma_{\min}$ , as illustrated in the top rows of Figure 11.

**Discrete endpoints.** For discrete data, conditional entropy remains bounded as  $\sigma \rightarrow 0$ . Empirically, across the discrete domains considered here, the entropy-rate exhibits an extended power-law regime

$$r(\sigma) \propto \sigma^\alpha \iff \log r(\sigma) = \text{const} + \alpha \log \sigma. \quad (49)$$

Equivalently, the log–log slope

$$s(\sigma) \triangleq \frac{d \log r}{d \log \sigma}$$

remains approximately constant and equal to  $\alpha$  throughout the low-noise regime.

As shown in the bottom rows of Figure 11, this regime appears as a linear segment in log–log coordinates with nearly constant slope. While the analytic mechanism differs from the continuous case, this structured low-noise regime similarly concentrates normalized mass toward the boundary.

Thus, both endpoint types exhibit boundary concentration under naive normalization, albeit for different structural reasons.

## B.2. Gated regularization

To control the boundary concentration described above (and in Section 3.3), we introduce a smooth multiplicative gate

$$g_{c,n}(\sigma) = \frac{\sigma^n}{\sigma^n + c^n}, \quad c > 0, n \geq 2, \quad (50)$$

which satisfies  $g_{c,n}(\sigma) \approx 1$  for  $\sigma \gg c$  and  $g_{c,n}(\sigma) \approx (\sigma/c)^n$  for  $\sigma \ll c$ .

For continuous endpoints, combining (48) with the small- $\sigma$  expansion yields

$$\left( \frac{d}{d\sigma} H[\mathbf{x}_0 | \mathbf{x}_\sigma] \right) g_{c,n}(\sigma) = \Theta(\sigma^{n-1}) \quad (\sigma \rightarrow 0), \quad (51)$$

so the gated profile vanishes at the boundary for  $n \geq 2$ . For discrete endpoints, the gate suppresses the empirical power-law regime in the same manner.

In both cases, the gate prevents collapse onto  $\sigma_{\min}$  while preserving mid-noise structure for  $\sigma \gg c$ . We use  $n = 3$  in all experiments.

## B.3. Relation to EDM weighting

For EDM-style training, a common loss weight is

$$w_{\text{EDM}}(\sigma) = \frac{\sigma^2 + \sigma_{\text{data}}^2}{(\sigma \sigma_{\text{data}})^2}. \quad (52)$$

The bounded factor in  $w_{\text{EDM}}(\sigma)^{-1}$  satisfies

$$\frac{\sigma^2}{\sigma^2 + \sigma_{\text{data}}^2} = g_{\sigma_{\text{data}},2}(\sigma), \quad (53)$$

showing that our gate recovers the same low-noise attenuation mechanism when  $n = 2$  and  $c = \sigma_{\text{data}}$ .

## B.4. Pivot selection

The pivot  $c$  identifies the upper boundary of the low-noise regime. Its definition depends on the structural behavior of the entropy-rate profile.

**Discrete endpoints (power-law boundary).** In discrete domains, the low-noise regime is characterized by approximate slope constancy in log–log space. Let

$$s(\sigma) = \frac{d \log r}{d \log \sigma}.$$

We define  $c$  as the largest  $\sigma$  such that  $s(\sigma)$  remains approximately constant over a contiguous region adjacent to  $\sigma_{\min}$ . Operationally, this corresponds to detecting the maximal stable log–log power-law segment and setting  $c$  at its upper endpoint. If slope stability cannot be reliably detected, we fall back to a curvature-based knee detector in log–log coordinates.

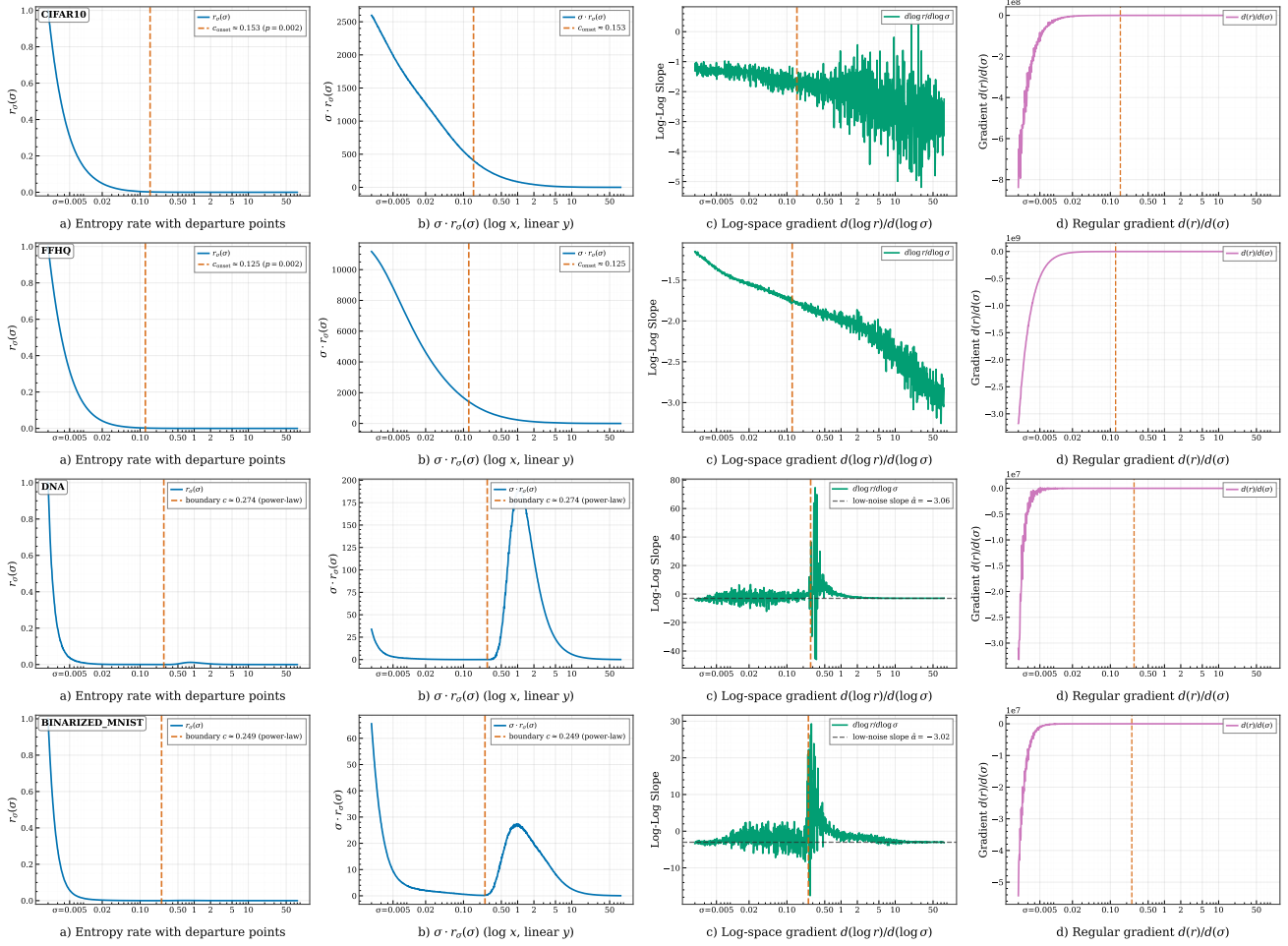


Figure 11. Entropy-rate profiles and their boundary structure for representative continuous (CIFAR-10, FFHQ) and discrete (DNA, binarized MNIST) domains. Top rows (continuous endpoints) display the predicted  $\sigma^{-1}$  growth as  $\sigma \rightarrow 0$ , which concentrates normalized mass near  $\sigma_{\min}$ . Bottom rows (discrete endpoints) exhibit an extended power-law regime, appearing as an approximately linear segment in log-log coordinates with near-constant slope. Vertical markers indicate the detected pivot  $c$ . In discrete domains,  $c$  corresponds to the upper boundary of the stable log-log power-law segment. In continuous domains,  $c$  marks the onset of the information-bearing region, defined via the first persistent rise of the normalized entropy-rate. These profiles motivate gated regularization to suppress boundary concentration while preserving mid-noise structure.

**Continuous endpoints (onset-of-information).** For continuous domains, the boundary corresponds to the transition from the near-zero high-noise regime to the information-bearing region. Let

$$\tilde{r}(\sigma) = \frac{r(\sigma)}{\max_{\tilde{\sigma}} r(\tilde{\sigma})}$$

denote the max-normalized profile. We define

$$c = \sup\{\sigma : \tilde{r}(\sigma') < p \text{ for all } \sigma' \geq \sigma\},$$

so that  $c$  marks the first persistent rise of the entropy-rate when scanning from high to low noise. We use  $p = 2 \times 10^{-3}$  and update  $c$  whenever the schedule is refreshed.

**Final allocation.** For discrete endpoints we set  $c = \hat{c}$ , and for continuous endpoints  $c = c_p$ . The gated allocation is then normalized as

$$\rho(\sigma) \propto r(\sigma) g_{c,n}(\sigma).$$

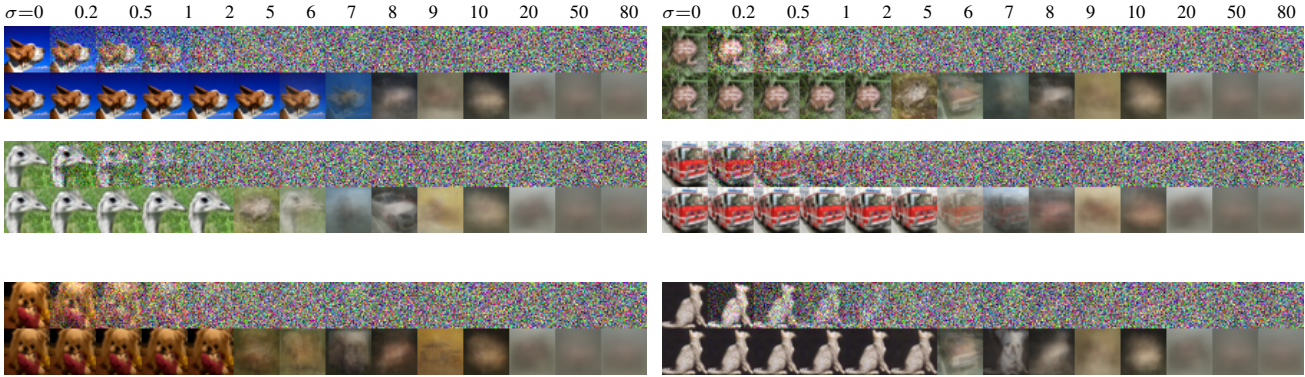


Figure 12. Extended visualization of the Bayes-optimal denoiser on CIFAR-10 under the Gaussian channel  $x_\sigma = x_0 + \sigma\epsilon$ ,  $\epsilon \sim \mathcal{N}(0, I)$ . Each block corresponds to a different training image  $x_0$ . Within each block, the top row shows the corrupted inputs  $x_\sigma$  across noise levels (values shown above), and the bottom row shows the corresponding Bayes-optimal denoised predictions  $\hat{x}^*(x_\sigma; \sigma) = \mathbb{E}[x_0 | x_\sigma]$  computed exactly under the empirical data distribution (Appendix A.2 and Section D.1). Visually, the extremes are near-trivial—at very small noise the denoiser is essentially identity, and at very large noise it collapses toward a dataset-level average—while the most pronounced qualitative changes concentrate in an intermediate range, matching the decision-window behavior discussed in the main text.

## C. Extended experiments

This section reports additional experiments.

## D. Implementation details

**Training setup and evaluation.** Our experiments reuse the EDM training pipeline (Karras et al., 2022) (architecture, preconditioning, optimizer, augmentations, EMA, and per-noise loss weighting). On continuous images, we keep the EDM objective fixed (including  $w_{\text{EDM}}(\sigma)$ ) and vary only the noise sampling distribution  $\pi(\sigma)$ ; on discrete domains, we use allocation-controlled runs with  $w(\sigma) \equiv 1$ , so the realized emphasis is  $\phi(\sigma) = \pi(\sigma)$ . We use the same U-Net family as EDM for each dataset: CIFAR-10/FFHQ/ImageNet-64 use the standard configuration, while MNIST and FashionMNIST reduce capacity by using the (1, 1, 1) channel-multiplier setting instead of (2, 2, 2) (all other choices unchanged); unless stated otherwise, remaining settings follow the dataset-specific EDM defaults. For DNA, we follow the dataset, preprocessing, and model architecture from DNA-Diffusion (DaSilva et al., 2024), keeping their training recipe fixed and varying only  $\pi(\sigma)$  (with  $w(\sigma) \equiv 1$  in allocation-controlled runs). We report Sei-FID as in (DaSilva et al., 2024). We report FID for images (Heusel et al., 2017) and Sei-FID for DNA (Chen et al., 2022); compute is measured in processed examples (kEx) unless a plot axis uses kimg. **Online schedule adaptation.** The online component only uses quantities already produced by SGD. At each step we record the sampled noise level  $\sigma$  and its denoising loss, accumulate these statistics on a fixed log- $\sigma$  grid, apply the low-noise regularization in Appendix B, and periodically refresh  $\pi(\sigma)$  by inverse-CDF sampling (Sec. 3 and Sec. 5). No extra forward passes are introduced beyond the training loss.

**Inverse-CDF sampling on a log-grid.** We tabulate a density over  $K$  grid points uniformly spaced in log  $\sigma$ , form its cumulative mass, sample  $u \sim \mathcal{U}(0, 1)$ , and map back to  $\sigma$  by linear interpolation between the two grid points that bracket  $u$ . Online updates use a warm-up of  $N_{\text{warm}}$  steps under  $\pi_{\text{base}}$ , an EMA with rate  $\beta$  applied to per-bin mean losses, and a refresh cadence of  $M$  steps.

**Software structure.** We implement INFONOISE as a scheduler component that is independent of the model architecture and objective. It exposes two operations: sample  $\sigma$  for the next update, and refresh  $\pi(\sigma)$  from accumulated loss statistics; optionally it exports the learned cumulative map  $u(\sigma)$  to build inference grids.

### D.1. Implementation details: empirical Bayes denoiser

**Optimal denoiser.** For the empirical prior (29), the posterior weights in (31) are proportional to isotropic Gaussian likelihoods,

$$\mathcal{N}(x; x_i, \sigma^2 \mathbf{I}_d) = (2\pi\sigma^2)^{-d/2} \exp\left(-\frac{1}{2\sigma^2} \|x - x_i\|_2^2\right).$$

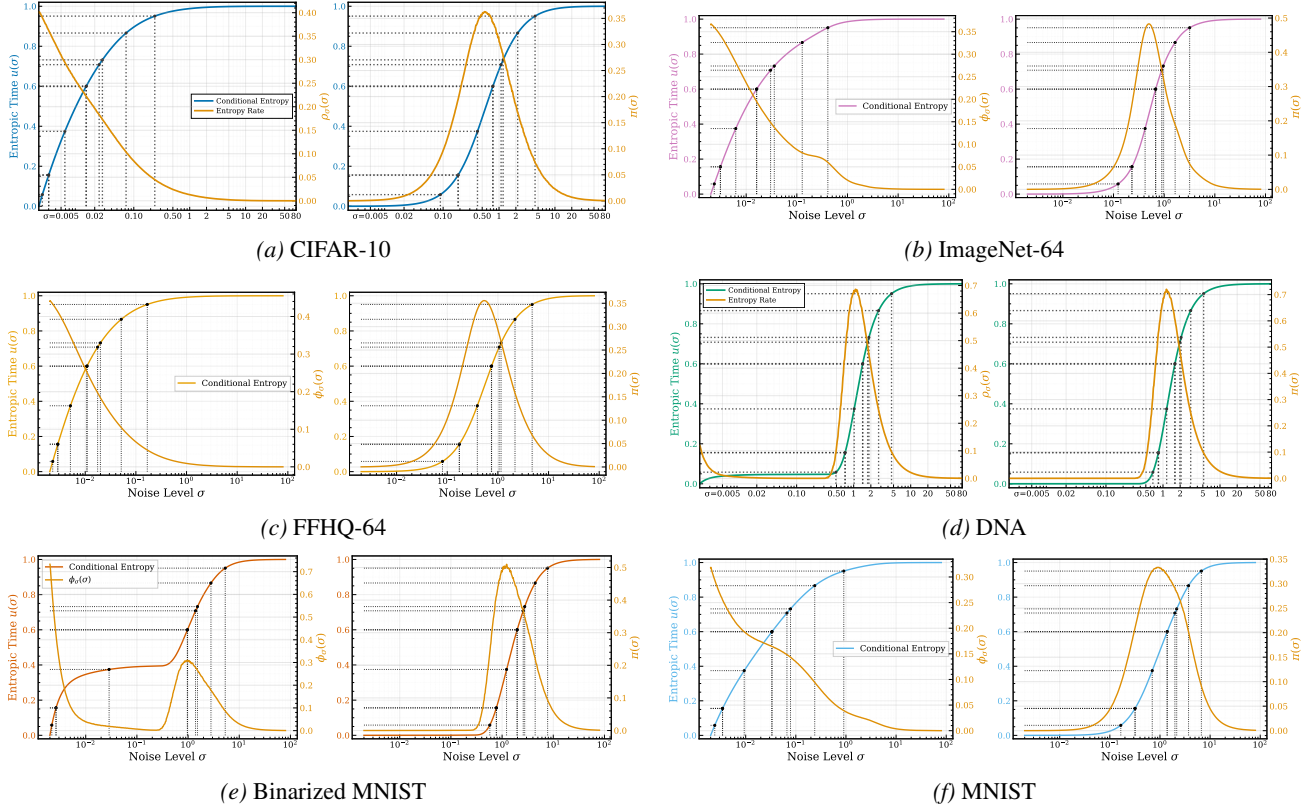


Figure 13. **INFO NOISE profiles across datasets.** Each panel applies the construction in Section 5 to a single dataset. **Left:** the normalized target allocation  $\phi_\sigma(\sigma)$  and its CDF  $u(\sigma)$  (used for inverse-CDF sampling). **Right:** the induced sampler  $\pi(\sigma)$  and the realized emphasis  $\phi(\sigma) = \pi(\sigma)w(\sigma)$  under the fixed per-noise weight  $w(\sigma)$ . We use EDM-style  $w(\sigma)$  for continuous images and  $w(\sigma) \equiv 1$  for discrete data. Together, the profiles show where training mass concentrates along  $\sigma$  and how low-noise behavior varies across representations.

Since the normalizing constant  $(2\pi\sigma^2)^{-d/2}$  does not depend on  $i$ , it cancels in the normalization and the weights reduce to a softmax over squared distances:

$$\ell_i(x; \sigma) \triangleq -\frac{1}{2\sigma^2} \|x - x_i\|_2^2, \quad w_i(x; \sigma) = \text{softmax}_i(\ell(x; \sigma)) = \frac{\exp(\ell_i(x; \sigma))}{\sum_{j=1}^N \exp(\ell_j(x; \sigma))}. \quad (54)$$

The Bayes denoiser (32) is then

$$\hat{x}^*(x; \sigma) = \sum_{i=1}^N w_i(x; \sigma) x_i.$$

**Stable evaluation (log-space).** We compute the weights via log-softmax to avoid overflow/underflow at small  $\sigma$ :

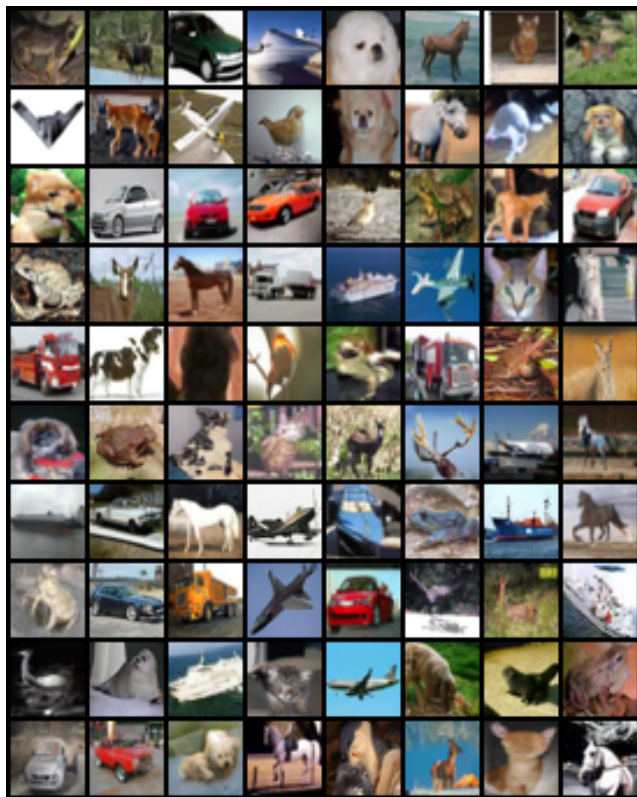
$$\log w_i(x; \sigma) = \ell_i(x; \sigma) - \log \sum_{j=1}^N \exp(\ell_j(x; \sigma)),$$

evaluating the log-normalizer with logsumexp (equivalently, using log softmax in autodiff libraries). We then exponentiate to obtain  $w_i$  and form  $\hat{x}^*$ .

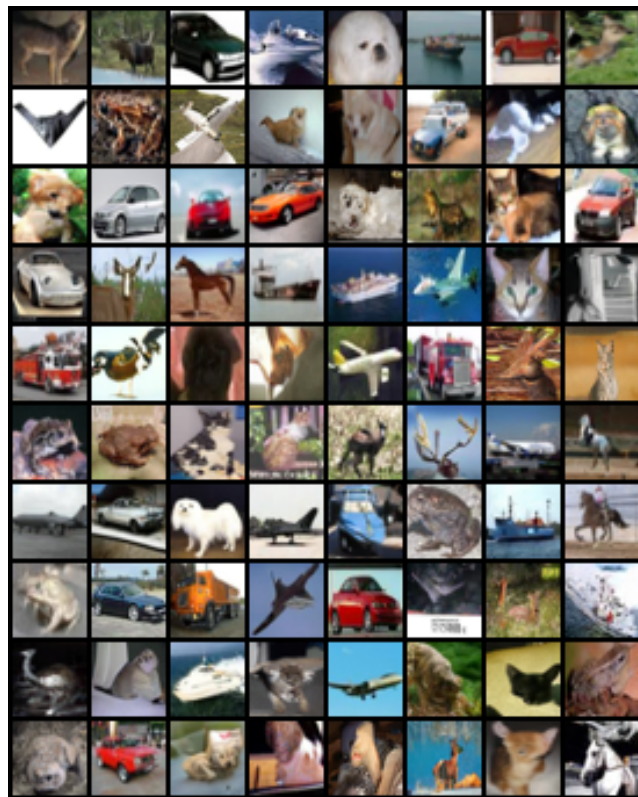
**Fast distances.** To compute  $\|x - x_i\|_2^2$  efficiently for many  $i$ , we use

$$\|x - x_i\|_2^2 = \|x\|_2^2 + \|x_i\|_2^2 - 2x^\top x_i,$$

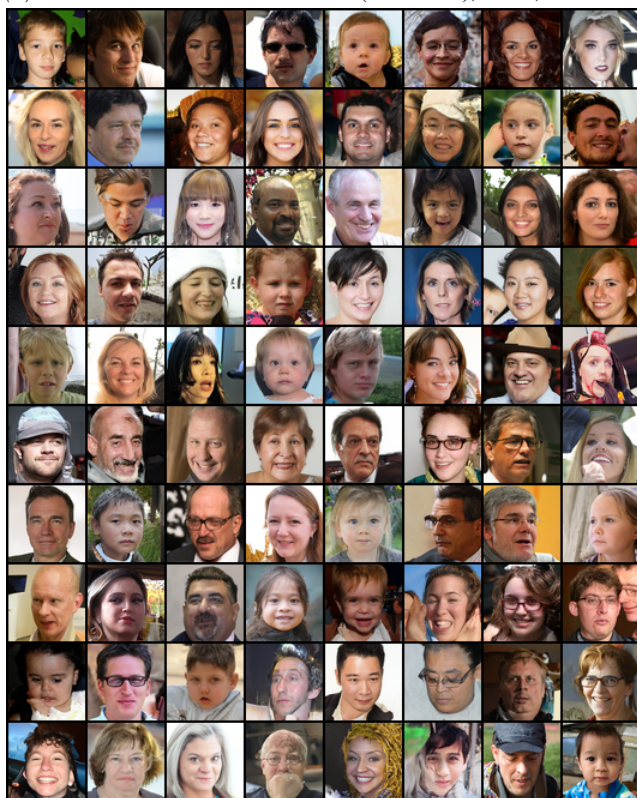
precomputing  $\{\|x_i\|_2^2\}_{i=1}^N$  once and reusing matrix products for the cross terms.



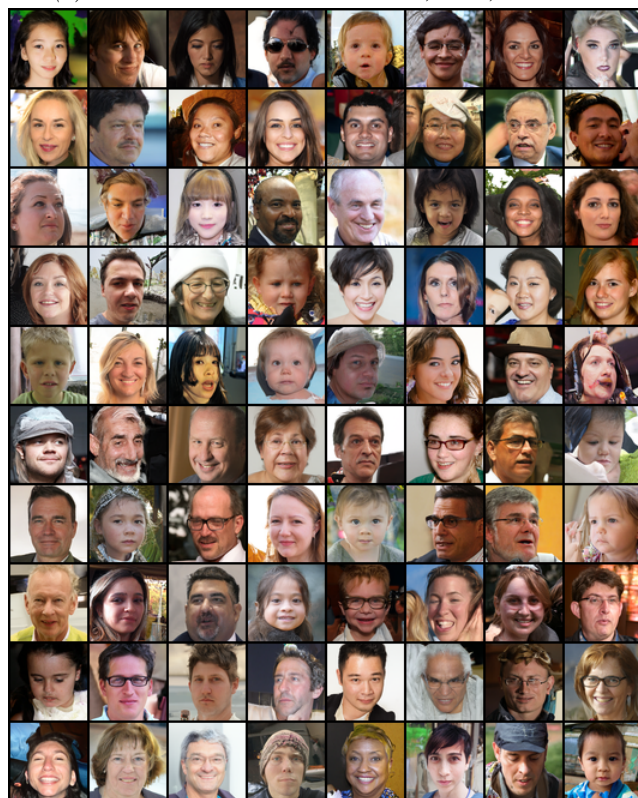
(a) CIFAR-10 @100k: INFONoise (InfoNoise), Heun, NFE= 35



(b) CIFAR-10 @100k: EDM baseline, Heun, NFE= 35



(c) FFHQ-64 @160k: INFONoise (InfoNoise), Heun, NFE= 80



(d) FFHQ-64 @160k: EDM baseline, Heun, NFE= 80

Figure 14. **Qualitative samples at matched training checkpoints.** We compare models trained with INFONoise versus the EDM schedule, evaluated with the same sampler/solver (Heun), the same inference grid, and the same NFE. Checkpoints are matched by training progress (CIFAR-10 @100k; FFHQ-64 @160k).